

AN SPM BASED TESTER FOR THE STUDY OF MICRO-CONTACTS

A THESIS

PRESENTED BY

NIKHIL JOSHI

TO

THE DEPARTMENT OF

MECHANICAL AND INDUSTRIAL ENGINEERING

In the partial fulfillment of the requirements

for the degree of

MASTER OF SCIENCE IN MECHANICAL ENGINEERING

IN THE FIELD OF

MECHANICS AND DESIGN

NORTHEASTERN UNIVERSITY

BOSTON MA

August 2010

Abstract

The testing of micro-contacts at low forces (below 1mN) is critical for understanding the contact evolution of MEMS contact-switches. Testing is achieved with a specially designed micro-contact-test assembly based on an AFM. The micro-contact-test assembly consists of a Si force sensor with an integrated micro-bump and a mating silicon pillar. Both sides of the contact can be coated with various combinations of metals to provide a wide range of metal-contact pairs for testing. When fabricated with different lengths, these force sensors cover a wide range of forces from 10 μ N to 1mN. Both force and resistance can be measured simultaneously during the contact tests. To protect the contacts from contamination, assemblies were first cleaned using Ar and O₂ plasmas, or UV/ozone, followed by testing under a constant stream of nitrogen. Cleaning efficiencies of Ar and O₂ plasma, and UV/ Ozone were compared by performing *in-situ* and *ex-situ* experiments on a variety of metal-pairs. Experiments were conducted on Au, Ru, Ir and V₂O₅-Au, and Au-Ni with three different compositions under different forces. It is proposed that integration of electrical properties of Au with the mechanical properties of Ru can promote an electromechanically sound and long lasting metal contact pair. Two strategies were followed to verify this proposition 1) using a layered stack of Ru of different thicknesses on Au for the entire test assembly 2) using a Au-coated force sensor over a Ru-coated pillar for conducting contact tests. The simulation results for the four-wire resistances of contacts using finite element analysis show good agreement with the recordings from the system.

Acknowledgements

I would like to thank all the people who have supported me mentally and academically while successfully completing this work.

First of all I am extremely thankful to my advisor Professor George Adams and co-advisor Professor Nicol McGruer for providing me with the opportunity to work on this project. Professor Adams has always been the source of inspiration for me. His solid knowledge in the field of contact mechanics helped me learn behavior of different metal-contact pairs. Professor McGruer was always supportive while constructing the system. His knowledge of electronics was vital in every aspect of the project.

I am thoroughly grateful to Dr. Lei Chen. Without his guidance and motivation, completion of this thesis would have been very difficult. His previous experience in testing of micro-contacts helped me rapidly learn different issues related with different metal-pairs and also while doing simulations using Ansys.

I also want to thank Ana Maria Pinto and Dr. Juan Aceros for guiding me while building the system. I was very fortunate to get the training on AFM from Peter Ryan. His role was very important while learning the calibrations required for the system.

The last but the most important acknowledgement belongs to Scott McNamara. He was always ready to help us and solve the problems related to different gasses and tube fittings. His help in clean-room has always been of a great value.

I specially appreciate the support given by all my friends and relatives.

Table of Contents

Table of Contents	4
Table of Figures	6
<u>Chapter 1: - Introduction</u>	
1.1 The Beginning of RF MEMS	8
1.2 An Overview of MEMS Switches	10
1.3 Types of Switches	12
1.4 Failure Mechanisms and Testing Background	14
1.5 Background	18
1.6 Contact Preparation	20
Cleaning Mechanism	22
1.6.1 UV/ Ozone Cleaning	22
Basics:-	22
1.6.2 Plasma Cleaning	24
1.7 Testing Background	27
<u>Chapter 2: - Set-Up</u>	
2.1 Purpose of the Set-Up	28
Contributions	29
2.2 Key Features of the Set-Up	30
2.2.1 JEOL SPM (Atomic Force Microscope)	30
2.2.2 Force Sensor	31
2.3 Mechanical Set-Up	34
2.3.1 Vacuum System and Plasma Source Generator: -	34
2.3.2 Lifting System: -	36
2.3.3 Nitrogen Flow Assembly for Ambient Control:-	37
2.4 Electrical Set-Up	38
Set-Up for Piezo	40
2.5 Testing Procedure	43
2.5.1 Procedure for Testing	45
Steps	45

2.5.2 Procedure for Plasma Cleaning	47
-------------------------------------	----

Chapter 3: - Simulation

3.1 Simulation of Pure Au-Au Contact	50
3.2 Simulation of Layered Ru	55

Chapter 4: - Discussion of Data and Results

4.1 Au_Au: -	60
Types of Failures Observed in Au-Au Contact During Cycling Tests: -	70
4.2 Ru_Ru & Ir_Ir	71
4.3 Au_Ru & Au_Ir	78
4.4 Vanadium Oxide	83
4.5 Au-Ni Alloys	85
<u>Chapter 5:- Conclusions</u>	87
<u>Chapter 6:- Future Work</u>	95

Appendix

A. Calculation for Nitrogen Flow Control	92
B. Calculations for Designing Roughing Hose Diameter	94
C. Vacuum Chamber	97
D. Lifting Structure	98
E. Tube and Holder Fittings for Nitrogen Flow Control	104
Bibliography	100

Table of Figures

Figure 1.1 MEMS Market Forecast	8
Figure 1.2 RF MEMS Switch Market Taken from (38)	10
Figure 1.3 Comparison of Technologies Taken from (39)	11
Figure 1.4 Classification of MEMS Switches	13
Figure 1.5 Contact Failure Due to High Pull-off Force	15
Figure 1.6 Contact Failure Due to Contamination	17
Figure 1.7 Plasma Cleaning Mechanism	25
Figure 2.1 Basic Functioning of AFM Showing Path of the Laser Beam and PD Segments Taken from SPM Manual (37)	30
Figure 2.2 SEM Image of Force Sensor	31
Figure 2.3 SEM Image of Pillar	31
Figure 2.4 Design of the Force Sensor and Pillar for Conducting Four -Wire Resistance Measurement Across Contact Area Taken from (40)	33
Figure 2.5 Nitrogen-Ambient Control	37
Figure 2.6 Two-Wire Resistance Measurement	38
Figure 2.7 Four-Wire Resistance Measurement	38
Figure 2.8 Electrical Set-Up	39
Figure 2.9 Schematic Diagram Showing Piezo Set-Up	41
Figure 2.10 Piezo Expansion Model	41
Figure 2.11 Schematic Diagram Showing Entire Set-Up	42
Figure 2.12 AFM Image of the Calibration Sample	43
Figure 2.13 Calibration Sample	43
Table 2.1: - Spceifications of the Force Sensors	34
Table 2.2: - Cycle-Frequency Table	49
Figure 3.1 Schematic Diagram of the Model of Simple Metal-Metal Contact	51
Figure 3.2 Meshing of Two $40\mu\text{m} \times 40\mu\text{m} \times 40\mu\text{m}$ Blocks in Contact With Each Other By Contact Area Having $a = 0.5\mu\text{m}$ Radius	52
Figure 3.3 Simulation Results Showing Resistance vs Thickness Plot	53
Figure 3.4 Simulated Voltage-Distribution for the Model With Real Geometry	54
Figure 3.5 Schematic Diagram of the Model Having Layered Structure	55
Figure 3.6 Simulated Contact Radius vs Force by Eid(27)	56
Figure 3.7 Simulated Contact Resistance vs Force for 10nm Ru Layered Over 500 nm Au and Model Represented by Equation (3)	58
Figure 3.8 Simulated Contact Resistance vs Force for 50nm Ru Layered Over 500nm Au and Model Represented by Equation (3)	58
Figure 3.9 Simulated Contact Resistance vs Force for 100nm Ru Layered Over 500nm Au and Model Represented by Equation (3)	58
Figure 3.10 Simulated Contact Resistance vs Force for 300nm Ru Layered Over 500nm Au and Model Represented by Equation (3)	58
Table 3.1 Simulated Contact Resistances for the Model With Real Geometry	55
Table 3.2 Measured Resistivity Values for Different Thicknesses	56

<i>Figure 4.1 Sample Signal Acquired from AFM</i>	61
<i>Figure 4.2 Au-Au Contact Resistance at Different Forces After ~10 Cycles</i>	63
<i>Figure 4.3 Au-Au Contact Resistance When Cycled at Particular Forces as Shown by the Bold Dots</i>	63
<i>Figure 4.4 In-situ Plasma Cleaning Experiment on Au-Au Contact</i>	66
<i>Figure 4.5 Resistance vs Force Diagram Showing Effect of 15min In-situ O₂ Plasma on Au-Au Contact</i>	66
<i>Figure 4.6 Au-Au Cleaning Effect of O₂ Plasma Cleaning on Pull-off Force</i>	68
<i>Figure 4.7 Au-Au Cleaning Effect of O₂ Plasma Cleaning on Contact Resistance</i>	68
<i>Figure 4.8 Au-Au Cycling Data Showing Resistance vs No. of Cycles</i>	69
<i>Figure 4.9 Au-Au Cycling Data Showing Pull-off Force vs No. of Cycles</i>	69
<i>Figure 4.10 Sliding Occurring at Au-Au Contact Due to Misalignment</i>	70
<i>Figure 4.11 Au-Au Contact Showing High Pull-off Force During Cycling</i>	70
<i>Figure 4.12 Au-Au Contact Ductile Separation</i>	70
<i>Figure 4.13 Ru & Ir Contact-Failures During Cycling</i>	71
<i>Figure 4.14 In-situ Plasma Cleaning of Ru-Ru Contact at 1 Hz</i>	72
<i>Figure 4.15 Ex-situ Ar Plasma Cleaning Effect on Ru-Ru Contact Resistance</i>	74
<i>Figure 4.16 Ru Contact Cycled at 500 μN After Ar Plasma Treatment</i>	74
<i>Figure 4.17 Ex-situ O₂ Plasma Cleaning Effect on Ru-Ru Contact Resistance</i>	75
<i>Figure 4.18 Cleaning Effect of O₂ Plasma on Ru-Ru at 100μN</i>	76
<i>Figure 4.19 Cycling Data of Ru-contact After O₂ Plasma Treatment</i>	76
<i>Figure 4.20 Comparison of Three Cleaning Methods</i>	77
<i>Figure 4.21 Cycling Data of Ir Contact After O₂ Plasma Treatment</i>	77
<i>Figure 4.22 Cycling Data of Au-Ir</i>	79
<i>Figure 4.23 Au-Ru Low-Force Contact Resistance Measurement</i>	79
<i>Figure 4.24 Au-Ru Cycled at 100 μN</i>	79
<i>Figure 4.25 Comparison of All Materials After O₂ Plasma Cleaning</i>	80
<i>Figure 4.26 Distribution of Contact Resistance Data of Layered Au/Ru</i>	81
<i>Figure 4.27 Comparison of Au-Ru With Layered Au/Ru</i>	82
<i>Figure 4.28 Au/ V₂O₅ Showing Effect of O₂ Plasma Cleaning</i>	84
<i>Figure 4.29 Au/ V₂O₅ Cycling Data</i>	84
<i>Figure 4.29 Au/V₂O₅ Cycling Data</i>	85
<i>Figure 4.30 Au-Ni Alloys' Contact Resistance Comparison After O₂ Plasma Cleaning</i>	85
<i>Figure 4.31 Au-Ni Alloys' Cycling Data Resistance vs No. of Cycles</i>	85
<i>Figure 4.32 Au-Ni Alloys' Cycling Data Pull-off Force vs No. of Cycles</i>	85
<i>Figure A1 Concentration Profile</i>	93
<i>Figure C1 Plasma Chamber</i>	97
<i>Figure D1 Lifting Structure</i>	98
<i>Figure E1 Drawing of the Clamp Fixed Inside AFM for Holding N₂ Tube Near Contact</i>	99
<i>Figure E2 Drawing of Tube Carrying N₂ Near Contact</i>	99

Chapter 1-Introduction

1.1 The Beginning of RF MEMS

MEMS technology is approximately forty years old and it has seen a wide improvement in its scope and usability. It covers wide applications, from pressure sensors, temperature sensors accelerometers switches, pumps etc. Figure 1.1 gives an idea of the different fields that are influenced by the MEMS technology (44). MEMS switches were first developed in 1980s and then for a long time it was in research phase. MEMS switch for microwave applications was first developed in 1990-91 by Dr. Larry Larson at the Hughes Research Labs (1). Even though the

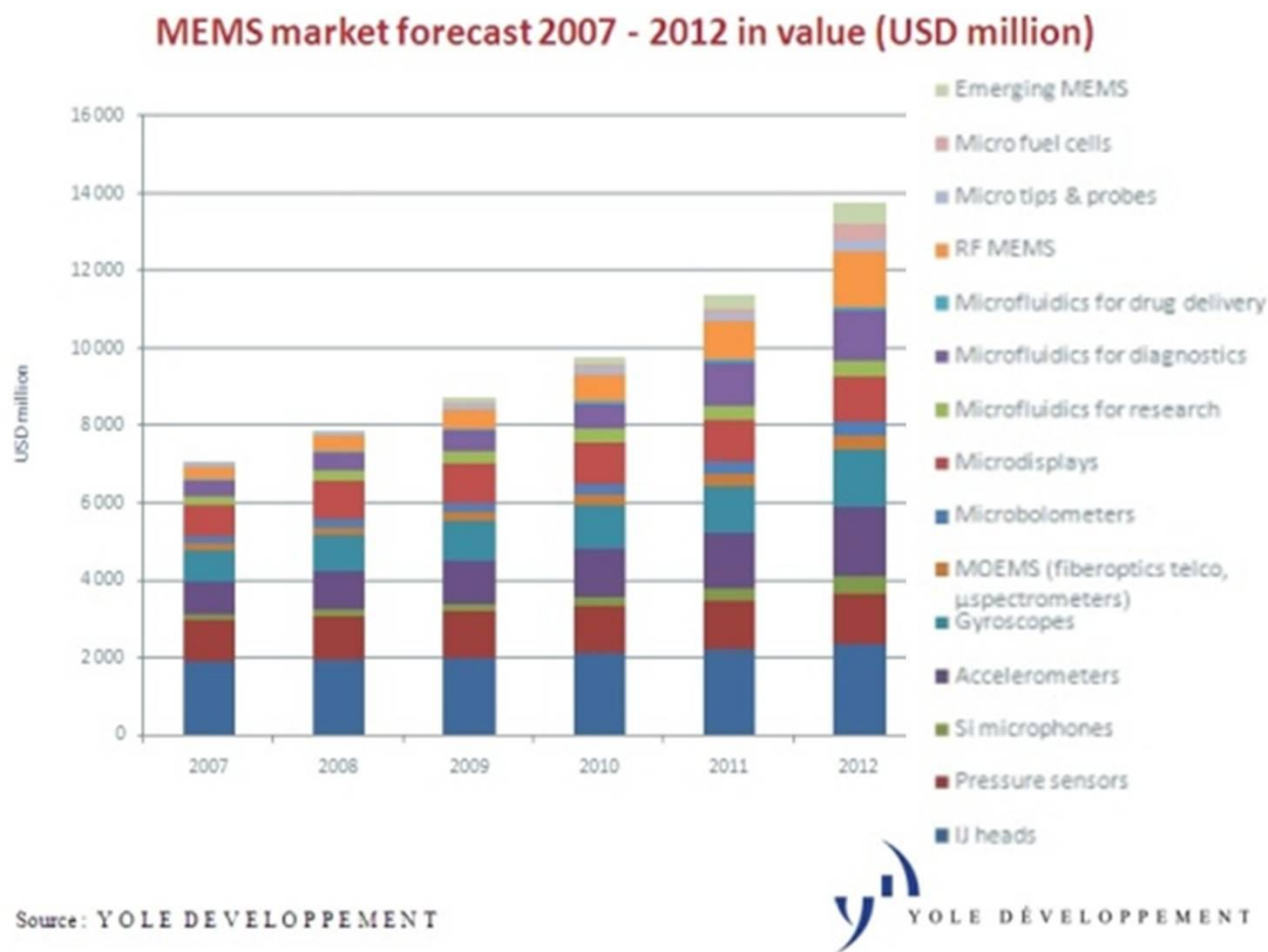
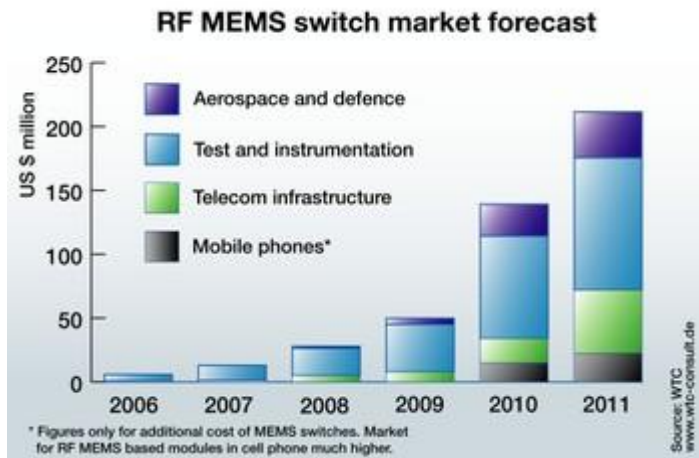


Figure 1.1 MEMS Market Forecast

technology had poor reliability and yield, it demonstrated promising performance than GaAs devices. This was the breakthrough in MEMS switch technology which caught the interest of different research groups and companies. The Rockwell Science Center gave rise to metal-to-metal contact switch while the one from Texas Instruments was of capacitive type. It took the mid and late 1990s to reach the MEMS switch-research at the university level when the University of Michigan, Northeastern University, University of California at Berkeley, MIT Lincoln Labs, and Columbia University got involved for improving the technology. By 2001 there were more than 30 companies such as Analog Devices, Motorola, and Samsung working in this area (1).

Main reason behind RF MEMS switch's rapid growth since the 1990s was that the semiconductor switching diodes could not improve more as compared to MEMS switches as far as the cutoff frequency was concerned. The cutoff frequency of silicon CMOS was improved from 500 MHz to 100 GHz, GaAs HEMT devices were improvement from 10-20 GHz to above 800 GHz while cutoff frequency of the InP p-i-n diodes could increase from 500 GHz in 1985 to 2000 GHz in 2001. This demanded some new technology which can be used at higher frequencies especially in defense applications. RF MEMS devices were proved promising even at 40,000 GHz with low-loss applications (1).

1.2 An Overview of MEMS Switches



MEMS systems are the combination of mechanical elements such as physically moving beams or diaphragms and electrical components used for actuation. Electronic components are fabricated using standard IC fabrication techniques while mechanical components are

Figure 1.2 RF MEMS Switch Market Taken from (38)

fabricated using compatible micromachining techniques for selectively etching or adding the structures to form the structures like beams. Figure 1.2 shows the increasing market value for RF MEMS in different applications. The trend that was predicted in 2006, as shown in Figure 1.2, seems to be in reasonable agreement with current market trends. It also gives us an idea of the increasing scope of MEMS switch market in different industries. It has found a big scope in defense applications and cell phone market because of their smaller size and higher cut-off frequency (2). These new system can be prototyped as one powerful station sending signals to the local cell phones that can act like the nodes of the network. The digital cellular and personal communications service (PCS) work at 0.9 and 1.9 GHz, respectively which consists of the range of frequency spectrum that is used for cellular purposes (3).

MEMS switches operating at RF frequencies do not actually have to switch at those frequencies. However it implies the frequency of electrical signal that is supported by these switches. Hence the micromechanical structures do the job of actuating the circuits when in physical contact and breaking the circuit when not in contact. This is the main reason behind higher isolation and

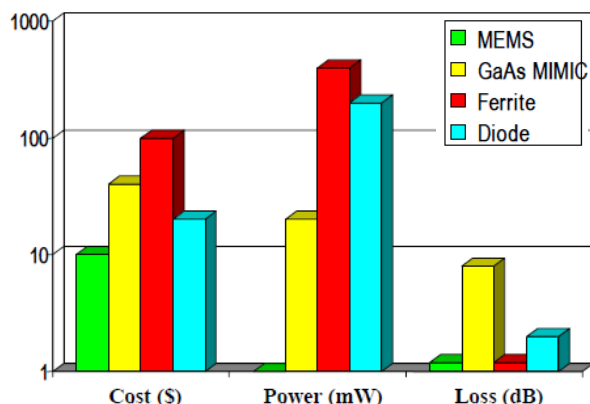


*Figure 1.3 Comparison of Technologies
Taken from (39)*

power consumption. MEMS switches are also recognized for their lower insertion loss. Figure 1.3 compares MEMS with different technologies for their cost, power consumption and loss. Despite of all these advantages, the RF MEMS has not yet able to replace its semiconductor counterparts because of the few shortcomings. Physical movement of the mechanical structures required for actuation puts limitation of switching speed of the switch. The electromechanical actuation time is typically many microseconds or greater, which is substantially longer than typical electrical time constants in semiconductor devices. Another major reason is the various types of failures involved in metal-metal contact. Stiction and contamination-failure are the most prominent types of contact failures. Stiction describes the phenomenon in which the top and bottom electrodes bond together by microscopic surface forces particularly occurring in metal-metal contact switches. It strongly depends on surface morphology. Contamination-failure is nothing but the rise in contact resistance due to different chemical reaction taking place on contacting surfaces during switching.

higher operating frequencies provided by MEMS switches. Another advantage of this technology is the low power consumption. Many of the RF MEMS devices under research are actuated electrostatically. So the current for actuation is required only while performing switching. This dynamic actuation lessens the

1.3 Types of Switches

‘MEMS switches’ is quite a broad term that consists of several types and designs. As explained in (1), it is possible to build at least 32 different types of MEMS switches using different actuation mechanisms, contacts and circuit implementations. A few of them will be discussed in this section. Figure 1.4 displays the five of the important characteristics that classify MEMS switches *i.e.* 1) Location of the RF circuit 2) Configuration of the RF circuit 3) Type of mechanical structure used for actuation 4) Type of contact 5) Actuation Mechanism MEMS switches are broadly categorized into following types depending on the location of RF circuit (3).

1. MEMS structures that are located outside the RF circuit *i.e.* RF extrinsic

Examples:- Tunable micromachined transmission line

2. MEMS structures that are located inside the RF circuit *i.e.* RF intrinsic

Examples:- Electrostatically operated shunt switch

3. MEMS structures that has RF function couples to the actuation *i.e.* RF reactive

Example: - Micromechanical resonator

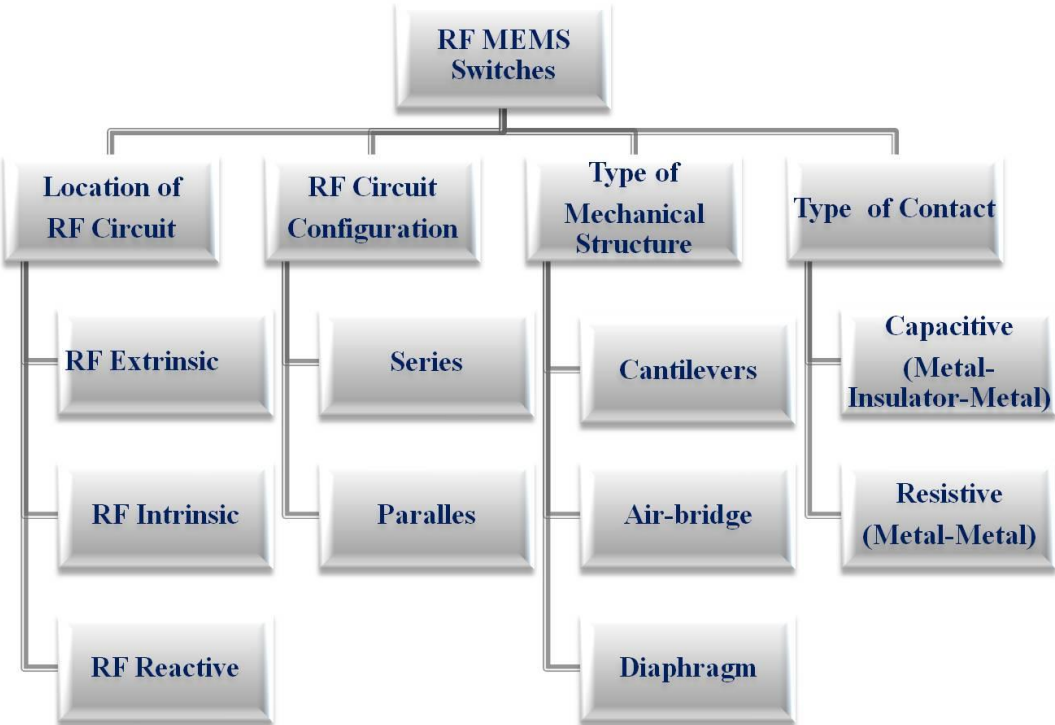


Figure 1.4 Classification of MEMS Switches

The most popular type is RF intrinsic where RF MEMS switches can operate at very high frequencies (from 1 GHz to 100GHz). Different configurations can be available for achieving these frequencies.

The switches are further categorized into following two types according to their RF circuit configuration as

(a) Series connection (b) Parallel connection

As mentioned above, the MEMS switches have some kind of physically moving mechanism for achieving switching action. This requirement further classifies the switches according to the type of mechanical structure used into the switch

(a) Cantilever:- As the name suggests, the actuation is accomplished with the help of a micromechanical beam having one end fixed and another end free to move.

- (b) Air Bridge:- A thin strip of metal and dielectric forming a bridge is fixed at both ends and suspended over free space in the middle.
- (c) Diaphragm:- The diaphragm is a thin film-like structure usually made of metal that is fixed at all of the edges while central area remains suspended.

Generally these are operated by using electrostatic actuation. Bias voltage applied between the cantilever or diaphragm and the base surface creates an electrostatic force of attraction and pulls down the suspended member at certain threshold voltage. Voltage can be reduced to bring it back to original position.

Another important classification of MEMS switches from contact point of view is

- (a) Capacitive: - It is also called as metal-insulator-metal and usually consists of membrane which gets pulled down due to the voltage applied between the control electrode and membrane. A dielectric layer provided on the control electrode keeps the membrane capacitively coupled. This helps in reducing impedance between the upper and lower electrodes (4).
- (b) Resistive: - These are normally metal-metal contact type switches either in the form of cantilever or membrane. Most of the types of switches those are currently popular or under research are of this type.

1.4 Failure Mechanisms and Testing Background

As explained in Chapter 1.1, MEMS contact switches have gained attention in the wireless industry considering their advantages over capacitive switches as well as solid state devices such as FETs and diodes. However none of the potential applications such as Tx/Rx antenna

switching, frequency band selection, tunable filters, and antenna reconfiguration etc. have been materialized in high volume products to a large extent because of reliability concerns. Most of the reliability issues are related to the metal contacts (4). Since MEMS contact switches incorporate physically moving components which contact each other at particular force, it becomes a challenging task to design a switch having such a metal-contact pair that will promise all the required electro-mechanical characteristics for more number of cycles ($\sim 10^9$). It is therefore necessary to understand the typical failure mechanisms occurring in micro-contacts during the switch-operation. Several attempts have been made in the past to study the micro-contact evolution. However Chen (5) and Majumder (6) are the two of the most important contributions. As it is studied by Chen (5), the most frequently observed types of failures in typical MEMS switches are

1. Failure to open and 2. Failure to close

Failure to Open (5): -

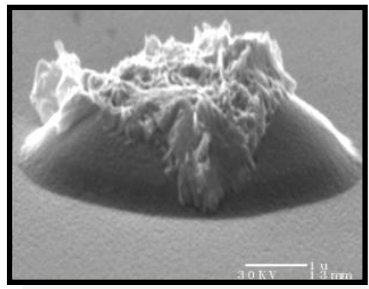


Figure 1.5 Contact Failure Due to High Pull-off Force

In most of the switches, the contacting members are deposited using techniques like sputter coating or evaporation, with some metal to achieve electrical continuity during switching. Even though they look very flat after deposition, their surfaces are covered with nano-asperities. During first few switching cycles a few asperities come into contact with the mating counterpart

resulting in multi-asperity contact with each asperity having very small contact area. Consistent application of force for few hundred or few thousand cycles causes these asperities to flatten out and regroup. This phenomenon increases the effective contact area. Cleaner surfaces, therefore,

can show strong adhesion because of their higher surface energies (1 to 3 J/m²) as compared to contaminated surface. The larger the contact-area the higher is the adherence force. Metals like Au which are soft and lesser reactive get relatively quickly flattened out during cycling. So the flat surface tries pull down the moving member of the switch. Hence the force of adhesion is also termed as pull-off force.

Current passing through any metal conductor increases its temperature because of the voltage applied and resistivity of contact-metals. Since, in microswitches, the contacting members have very small cross sectional area, even small increase of current cause significant increase in temperature and soften the nano-asperities. During switching action, the surface morphology undergoes some changes due to the softening and hence contact area increases. Pull-off force may eventually increase as explained above. Even the small voltage like 430mV can increase the temperature of Au micro-contacts up to 1063⁰ C and melt it. This melting makes the micro-welding of contact spots and separation becomes difficult. The load applied to the microcontact causes plastic yielding of the contact-metal. As the switching progresses, the cyclic loading and unloading transfers some material from one side to another and reduces the scope of separation. Ductile separation is another type of the failure occurring in metal-contacts due to higher applied forces or higher contact adhesion. Both of these causes can rupture the micro-contact and deform it plastically. During unloading, instead of pure separation, plastic yielding imposes neck formation across the contact and nano-wires can be formed. These nano-wires or micro-bridges keep the moving member electrically connected to the stationary part. Plastic yielding can also cause material transfer and makes the switch unable to separate.

Failure while Hot Switching: - Usually current is allowed to flow across the contact only when the switch is closed. Hot switching refers to the mode of operation when current is continuously

flowing across the contacting members even though they are in open state. High voltage applied across the contact can cause arcing. This leads to the softening of contact-metal especially Au. The contact fails due to increase in stiction or contact welding.

Failure to Close (5): -

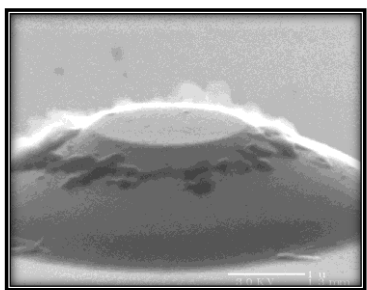


Figure 1.6 Contact Failure Due to Contamination

This is mainly referred to as excessive increase in contact resistance. This may occur due to the surface films present after microfabrication processes. Normally these films are few nanometers thick and can break down during cycling if slightly higher force ($> 100 \mu\text{N}$) or higher current is applied. However the refractory metals like Ru, Ir have higher affinity for the

hydrocarbons and they can also attract carbonaceous molecules from the atmosphere and act as catalyst. These reactions build serious contamination and electrical resistance increases that makes. The best way to prevent this kind of failure is to modify microfabrication processes so that surface films will not exist. Methods such as plasma cleaning or UV/Ozone cleaning are must before packaging to remove any traces of contaminants left during fabrication steps. Controlling the ambient during packaging by using gasses like N_2 or Ar is very crucial for avoiding contamination.

Pitting and hardening of the metal contact area is another reason behind the increase in contact resistance. As the two members coated with metal hit each other repeatedly at the same spot, strain-hardening occurs at local contact-spots. This reduces contact area and eventually increases contact resistance.

1.5 Background

All the modes of failure mentioned above are interconnected with each other and switch doesn't always fail only because of one single reason. Different theories and observations made during the experiments help us understand the causes of failure. Usually the MEMS contact-switches that survive 10^8 to 10^9 cycles without significant increase in contact resistance ($< 1 \Omega$) or contact failure while operating at lower forces ($\sim 100 \mu\text{N}$) are considered as reliable for the commercial applications. Au has always been the favorite metal for contact switches because of its low resistivity and nobleness. It has been widely used in the switches developed by different companies such as Motorola, HRL, Omron and universities for e.g University of Illinois, Northeastern University, University of Michigan, Lincoln labs at MIT(1). However contact-stiction occurring in Au contacts has put some limitation on the life-time and reliability. Au is also a very soft metal. Its softening temperature i.e. 100°C is achieved by applying merely 70mV across the contact. Any temperature higher than that can lead the switch fail to open either because of stiction and material transfer. Different groups have also tried materials such as Ru, Rh, Ir alloys for avoiding the stiction problem but these metals are not easy to handle during microfabrication steps. If the deposition conditions are not maintained, the thin films develop high residual stress and buckle the original structure. These refractory metals also have strong affinity for hydrocarbons. Hence, unlike Au, they get contaminated very quickly. Higher electrical resistivity and material hardness are also two of the characteristics that make switch-designing a tough task. So, the companies or research institutes have to make several improvements in the switch design and fabrication for improving the life time for using Au as the contact metal. These designs include ball-grid array and dimple designs (7), collapsing type cantilevers (8), multiple contact-points by Duffy *et al* (1), and corrugated diaphragm (9), macro-

contact spots by Schimkat *et al* (1), and self cleaning lateral actuation (10). However research has also been going on to find more reliable metal-contact pair that can replace gold so that the switch design can be simple. Ru (9), Ir (11) Au-Ni alloys by Schimkat *et al* (1), Ru, Rh (12), palladium multilayer structures (13), Rh and Au-Ni (8), platinum by Duffy *et al* (1) are some of the examples of them.

For testing these materials under different conditions special test-facilities are required. These test facilities generally use AFM (14), (5), nano-indenter (11), (15),(16),(17) or pico-indenter (8) for measuring/controlling the force applied on the micro-contact. However most of them have failed to test the contacts at lower forces. Cycling the contacts for more than 10^6 cycles is also an important requirement of the facility. Although the systems constructed by Ma *et al* (8), Yunus (16) and Kwon(11) are really good for comparing different material pairs, they have not performed any cycling test, which does not confer the long term performance of respective materials. Also, Ma *et al*(8) and Yang (14) directly use the upper cantilever from the commercially available switches which puts limitation on using various metals for the upper side of contact. On the other hand the test-stations by Gilbert *et al*(15) can investigate different metal-metal pairs and perform cycling tests as well. However, the lack of ambient control shows very rapid contamination-failure. The contact resistances recorded are on higher side because of the implementation of two-point probe method instead of four-point probe. Kwon *et al* (11) have compared a different metal-contact but again, the lack of cycling tests and ambient control does not provide us with the entire picture of contact-evolution data.

It is therefore the focus of this research work is to build an efficient system for studying the evolution of micro-contacts and suggest an electro-mechanically reliable metal-contact pair for MEMS microswitches.

1.6 Contact Preparation

Plasma treatment of solid surfaces has received a big attention in recent years. It is implemented in most of the industries for improving reliability. Contamination being one of the major causes of micro-contact-failure, surface preparation is very important before packaging.

These contaminants can be removed either by wet processes or dry processes. However wet processes incorporate the usage of different hazardous chemicals (18), (19). This makes the task of waste disposal challenging. The processes thus become lengthy and expensive. Also, higher material removal rate and different physical properties of the fluids such as surface tension, viscosity cause severe damage to the delicate MEMS cantilevers diaphragms etc. In general, wet chemical processes are used to clean up the contaminants having thickness in the range of $10\mu\text{m}$. It is further treated by plasma techniques to reduce it up to atomic level. However, the wet chemical process shows some problems, such as the disposal of toxic chemicals due to the vast usage of chemicals, re-contamination from the chemicals, and residues left behind in high-aspect-ratio-structures (20). In this context, cold plasma technology represents an efficient alternative, which has been object of increasing attention properties of adhesion, unless some form of surface pre-treatment is involved (18). Gas plasmas have higher degree of cleanliness than that achieved by solvent cleaning plasmas. For the MEMS technology, a cleaning process having following properties is recognized as good and reliable process.

1. Fast material removal rate
2. No damage to the original structure
3. Process that provides higher degree of cleanliness

4. Safe and easy to remove by-products after treatment

5. Cost effective

Since plasma cleaning technology can fulfill these requirements, it has become more popular in recent years. Next sections explain the basic mechanism of plasma cleaning and UV/Ozone cleaning, and previous work done in contact cleaning.

A given solid surface can be considered in the form of layers of different materials which cause the contact resistance to increase beyond limits. These contaminants can be natural or process-dependent. Their thickness depends upon type of material itself, or processes used during micro-fabrication and sample handling (18).

Typically a given contaminated surface exposed to the atmosphere should have the layered structure as follows.

For example a strip of metal, glass surface or a silicon wafer, on its surface, can have:-

1. Natural Contaminants:- These are present due to long exposure to the ambient atmosphere(18),(21). They include

- Physically or chemically adsorbed water
- Natural contaminants such as oxides growing on metal surface
- Different species containing carbon for e.g. CO₂, CO etc.
- Simple hydrocarbons

2. Process-born/ Technological Contaminants:- These are present due to some micro-fabrication processes, improper sample handling. They include

- Residual grease left after wet cleaning
- Oil
- Complex hydrocarbons

Cleaning Mechanism

1.6.1 UV/ Ozone Cleaning

The study of UV/Ozone for cleaning the surfaces began in 1972 when D. A. Bolon and C.O. Kunz (22) found a method for the removing thin films of photoresist polymers. They showed that the surface gets cleaned when polymeric films are exposed to the UV light in the presence of air. This process was further examined for a variety of photoresist polymers and non-photoresist polymers and on a variety of substrates. R.R. Sowell *et al*, in 1974, investigated the effects of prolonged exposure to UV light in ambient air and in vacuum under pressure of 10^{-4} torr with the presence of oxygen. They were able to clean the Au surface and glass slides by exposing it to UV/Ozone for 15 hours. The actual use of UV/Ozone for cleaning purpose started from early 80's with the manufacturing of liquid crystal display LCD. Lately it is used in most high-definition electronic products for cleaning and modification purposes.

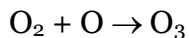
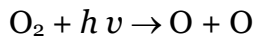
Basics:-

As demonstrated by the experiments conducted by (22) only the light that is absorbed can be used for cleaning. So it most important to choose the proper spectrum of wavelengths for effective cleaning experiment.

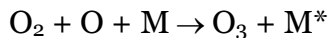
Ozone is created at the 184.9nm level, while the presence of 253.7nm helps in the destruction of ozone. If both are present, then there is a constant creation and destruction of ozone, which in

turns encourages the formation of atomic oxygen, an exceptionally strong oxidizing agent. The sequence of reactions normally proceeds in following manner.

When an oxygen molecule receives energy by absorbing light at 184.9nm wavelength, it dissociates into monoatomic atoms. These atoms being unstable attack an oxygen molecule to form ozone, O₃.



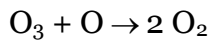
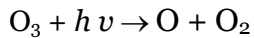
The last reaction requires a third molecule to take away the energy associated with the free radical O and O₂, and the reaction can be represented by



The overall reaction between oxygen and ozone formation is:



Absorption of the wavelength 253.7nm helps in destroying the Ozone as follows.



The radiation at 253.7nm is not absorbed by oxygen so it does not contribute to ozone generation but it is absorbed by the hydrocarbons and also by ozone. Ozone gets destroyed after this absorption. Therefore, when both wavelengths are present, ozone is continuously being formed and destroyed. An intermediate product of both the formation and destruction processes is atomic oxygen, which is a very strong oxidizing agent. These oxidation reactions result in the formation of simple products like CO₂ and H₂O which desorb from the surface.

UV/Ozone cleaning has many applications. It can also be effective in cleaning water. The cleaning combination has shown the ability to clear water of toxic contaminants like ethanol, medical waste, and pesticides. Further tests on the subject of water cleaning with UV/Ozone have shown that using the two in conjunction is more effective than using either alone.

This method of cleaning works well on many surfaces provided the proper setup is used. As long as the surface to be cleaned has had gross contamination removed, is properly exposed to the light, and given the optimal amount of time to be cleaned, UV/Ozone cleaning will produce a nearly completely clean surface by any measurement.

1.6.2 Plasma Cleaning

Plasma can be defined as a partially or wholly ionized gas with a roughly equal number of positively and negatively charged particles. Plasma is artificially generated using high voltage, high temperature arc which is the basis for the corona discharge process and for the plasma torch used to vaporize and redeposit metals. When a gas-atom is ionized due to high voltage, the collision of high energy particles knocks electrons out of their orbits. This results in very reactive free electrons as well as the characteristic 'glow' associated with plasma. The color of the glow depends on the type of gas or mixture of gases used while generating plasma. Gas plasma, thus, consists of activated species that include atoms, molecules, ions, electrons, free radicals, metastables and photons in the short wave ultraviolet (vacuum UV *i.e.* VUV) range. Under atmospheric pressure, the ionized gas is very hot and reactive. It can damage the device. However for industrial cleaning and surface treatment purpose low temperature and low pressure (0.1 to 2 torr) plasmas are preferred. Even though electric discharge produces the particles having high temperature (few thousand Kelvin), the low temperature of the ions and neutral particles reduces the overall temperature of plasma-pool down to few hundred kelvin.

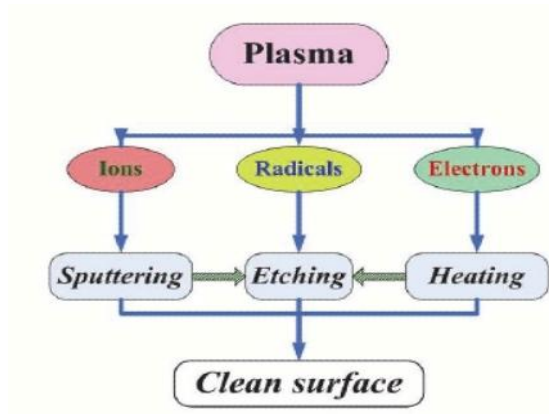
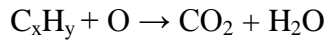


Figure 1.7 Plasma Cleaning Mechanism

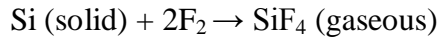
Plasma being the fourth state of matter consists of free ions, electrons and radicals. Their interactions with the metal surface include three phenomena. *Figure 1.7*, taken from (18), illustrates the cleaning mechanism.

bombardment. To avoid undesirable exothermic formation of metal carbides or polymerization of organic contaminants, temperature should be limited to below 60 °C. Physiosorbed particles or lightly bonded contaminants get removed during this phenomenon. Thin layer of water particles also gets evaporated.

- **Heating:** - Surface immersed in the plasma gets heated due to plasma radiation and electron/ ion bombardment.
- **Etching:** - Plasma cleaning by etching is the most important form of cleaning in which the atoms and radicals from plasma chemically react with the contaminants and breakdown the complex compounds into much simpler bi-products. This effectiveness of phenomenon largely depends on the type of gas-plasma used. The active species in argon-plasma mainly knock out the contaminant molecules from the metal surface. Even though the electrons and radicals may involve in some chemical reactions, it is not very strong and effective. The plasma becomes very effective, economical, safe and quick with the use of oxygen gas. The vacuum ultraviolet (VUV) energy can break the strong bonds of hydrocarbons or oxide species that are present on the surface. Some of these bonds can be represented as C-H, C-C, C=C, C-O, C-N etc. Highly reactive oxygen radicals further attack these broken bonds to form simple products such as H₂O, CO, CO₂. These compounds have higher vapor pressures and can be further sucked out of the vacuum chamber for maintain the plasma conditions leaving a clean surface (23).



The stronger gases such as NF_3 , SF_6 or F_2 are highly reactive with Si. These gasses form the compounds with Si to from the compounds like SiF_4 . Since almost all of the MEMS devices are fabricated by using Si for the base structure, these gasses practically etch the original structure and damage it. Hence the use of these gasses for plasma cleaning is prohibited



- Sputtering: - An additional voltage ($< 30V$) applied between the plasma and surface of a conductive object accelerates the ions from plasma improving the material removal rate. This is called as floating voltage (18). Since the sputtering yield strongly depends on nature of the surface and type of contaminants, cleaning by sputtering is not very effective. Moreover, this phenomenon is also associated with the bulk material removal damaging the original structure. Hence, its usage is limited to applications where plasma cleaning by heating and etching is not very effective and contamination is severe. The advantages of bombardment are that it is not a chemical reaction, and it cleans the surfaces of parts without leaving any oxidation. The result of this cleaning effect is a pure surface made up entirely of the substrate material. In our tests with plasma cleaning downstream plasma is directly focused on the samples. Also, since the samples are handled very carefully during microfabrication stages, the level of contamination is not very severe. We have not applied any floating voltage to accelerate the ions. So, cleaning by sputtering mechanism is avoided during our experiments.

1.7 Testing Background

Research preformed by (24) has illustrated that the efficiency of nitrogen plasma is between the oxygen plasma and argon plasma. It is likely that the free radicals generated in the nitrogen plasma are less effective in chemically changing the surface. Contact angle (the angle at which a liquid meets the surface), is the measure of the wettability of the surface. If the angle θ is less than 90 the liquid is said to wet the solid. If it is greater than 90 it is said to be non-wetting. A zero contact angle represents complete wetting. A contact angle test performed by Kim *et al*(24), to investigate the changes in wettability of the surface after plasma treatment revealed that the oxygen-based plasma has a greater impact on the contact angle than either nitrogen or argon. The contact angle trend that is presented by Kim *et al* (24) is: O₂ plasma > N₂ plasma > Ar plasma. From the materials' and applications' perspective, the surface contact angle is not the only consideration but it helps in comparing the efficiency of plasmas of different gasses. If the sample is sensitive to surface oxidation, then plasma conditions that offer no or lower oxygen concentrations may be desirable (24). It has also been reported that oxygen atoms rather than excited state oxygen molecules are the primary reactive species. They are strong enough to remove photoresist (20). According to (20), if the contamination is not completely removed prior to metal-deposition can cause reliability concerns. The ashing rate generally increased with increasing processing temperature, oxygen gas flow rate, RF plasma power, and plasma exposure time. Belkind and Gershman (18), and García (19) reveal that Ar plasma is effective in surface cleaning but due to the absence of reacting species it is lesser effective than O₂ plasma. As stated in (21), oxygen plasma was ~six times effective for reducing contaminants, as compared to Ar plasma. However if the metal to be cleaned is easily oxidized, such as silver, argon plasma is preferred.

Chapter 2- Set up

2.1 Purpose of the Set-Up

As we have learnt from chapter 1, several attempts have been made to study the micro-contact in different manners. Different set-ups have their own advantages but none of them is able to perform all the tasks necessary for studying microcontact. An ideal set-up is supposed to have the following attributes

- Simultaneous acquisition of force applied and electrical resistance across the contact
- Four-wire resistance measurement
- Ambient control to isolate the contact from contaminants
- Ambient control to test the effects of different gasses on switch-reliability
- Set-up for contact cleaning by using different methods such as UV/Ozone, and plasmas of different gasses.
- Hot-switching and cold-switching ability
- Ability to perform cycling tests
- Ability to test different material pairs

The test facility used in this research is constructed with the intent of having all of the aforementioned features.

Contributions

The test set-up that is explained in this chapter is the outcome of the contributions made by different individual working with our research group. This section is dedicated to acknowledge all such efforts. The original concept of using JEOL SPM for performing micro-contact tests was used by Chen *et al* (41). Dr. Guo modified the force sensor and designed it to have the fixed-fixed beam structure (Figure 2.2) with trenches for performing four wire resistance measurements. We have used these force sensors for performing experiments. For avoiding the sheet resistance effect arising from vertical pillar-walls (41), Dr. Chen altered the pillar design to make it trapezoidal as shown in figure 2.3. Dr. Aceros and Dr. Lei Chen have performed several experiments on micro-fabrication techniques and deposition procedures for perfecting the structures. It should also be noted that different components of plasma-cleaning system such as vacuum chamber, flow controllers for the gasses, gas tube connections, and lifting structure for the plasma system was designed by Ana Pinto. The contribution of Dr. Aceros during system-assembly is worth mentioning. The LabVIEW software used in this work was developed by Suchit Shah and further modified by Dr. Chen to make it more user-friendly. I was privileged to work with Ana Pinto during the initial phase of designing the different components of vacuum system. I further assisted Dr. Aceros while assembling the vacuum system and constructing the set-up for four-wire resistance measurement. Most of the experiments on cleaning methods and contact-resistance measurements that are explained in Chapter 4 were performed by me under the supervision of Dr. Chen (unless specified).

2.2 Key Features of the Set-Up

2.2.1 JEOL SPM (Atomic Force Microscope)

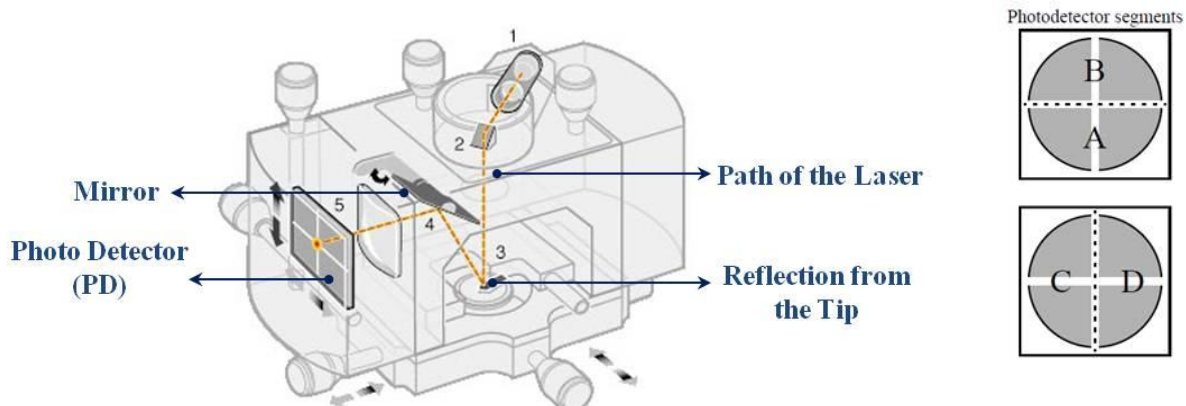


Figure 2.1 Basic Functioning of AFM Showing Path of the Laser Beam and PD Segments Taken from SPM Manual (37)

Atomic Force Microscopy (AFM), which is a kind of scanning probe microscopy was initially developed to overcome the problems involved in scanning tunneling microscopy (STM). As the name suggests, the most important part of SPM is the probe. This probe, usually located at the end of micro-cantilever, is called as tip. All the modern AFM cantilevers are microfabricated from Si or Si_3N_4 . A laser beam is focused at the end of the tip from where it gets reflected to the photodetector (PD). The position of the laser spot on PD is converted into voltage. Hence any change in location of the laser spot is represented as change in voltage by PD. As shown in Figure 2.1, the square shaped PD is divided into four quadrants. The combination of top two and bottom two are called as B and A respectively. The amplified differential signal from these two sections is called as A-B signal. This signal measures the vertical laser movement. Similarly the combination two quadrants from left and two from right are termed as C and D respectively. The C-D signal is the amplified differential signal of these two and it provides the measure of torsion. As the tip moves on the surface under study, it encounters deflection depending on the irregularities and grain structure of the surface. Tip-deflection causes rotation at the end of the

AFM cantilever which changes the path of the laser beam. This change of path is sensed by the photodiode in terms of change in voltage. Since an AFM tip is in the form of cantilever beam having some spring-stiffness *i.e.* ‘K’ (depending on the material and dimensions of the cantilever) it can be used to measure the forces responsible for bending the cantilever. Tip-deflection depends on the rotation due to bending which eventually is in linear proportion with the displacement of the laser spot on PD. For converting the changes of PD-voltage into displacement, ‘ δ ’, A-B signal is required to be calibrated. The calibration procedure is explained in section 2.5. The spring stiffness, ‘K’, when multiplied by spring deflection ‘ δ ’ gives the total force acting on the beam. Hence, for our experimentation purpose, A-B signal that measures vertical tip-deflection becomes the most important signal. We have used *JEOL SPM* for detecting laser signal as mentioned above. Next section describes the tip used for deflecting the laser beam and measure the force applied at contact.

2.2.2 Force Sensor

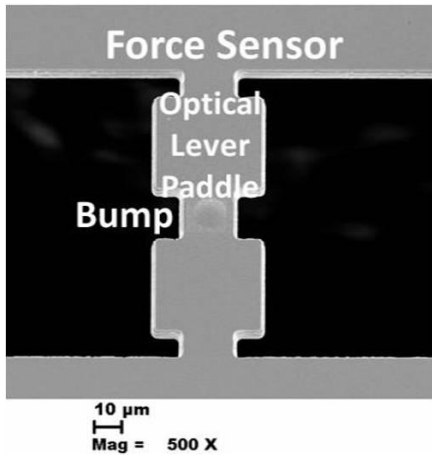


Figure 2.2 SEM Image of Force Sensor

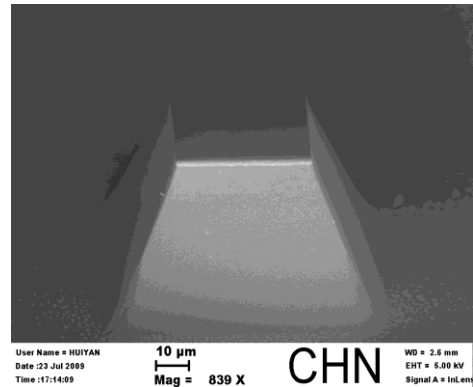


Figure 2.3 SEM Image of Pillar

The functioning of AFM requires only the vertical deflection of laser spot to measure the force acting on the beam. Any AFM cantilever itself can act as a force sensor as explained in previous section. However, the prime requirement of the entire set-up is the simultaneous acquisition of force and resistance data. Chen (5) has performed extensive research on contact evolution by using specially fabricated cantilevers with a microbump at the tip. The tips used in this set-up are further modified so as to have the doubly fixed configuration and a microbump as shown in figure 2.2. This doubly fixed design provides us with following advantages.

- No sliding: - The cantilevers used by (5) had the microbumps at the tip. For acquiring the data in the high force regime ($\sim 500 \mu\text{N}$) very large deflection are needed to be given while using cantilevers. This large vertical displacement is also associated with the large angular displacement at the end of cantilever that forces the microbump to slide on contact surface. This sliding creates unwanted changes in surface morphology. This ‘contact-scrub’ can reduce the contact resistance. Furthermore, the metallic films which are sputter-coated on the bump are very thin; they can be destroyed at higher forces during sliding.
- Four-wire resistance measurements: - Four-wire measurement is an accurate way of measuring contact resistance as explained in section 2.4. Figure 2.4 shows the manner in which the four contact-points are provided on the test-structures. A doubly fixed beam can offer two contact points on the upper side. Trenches are etched on the substrate as shown in figure 2.4. When the tip is coated with a particular metal, these trenches help isolate the two sides of the beam and thus avoid any sheet resistance involved during the measurement. This feature is very difficult to incorporate while using a cantilever

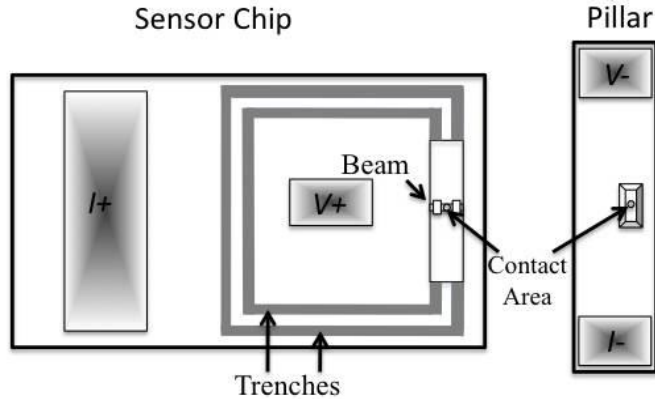


Figure 2.4 Design of the Force Sensor and Pillar for Conducting Four -Wire Resistance Measurement Across Contact Area Taken from (40)

design. Figure 2.7 illustrates the actual electrical set-up used for performing four-wire resistance measurements.

- Angular deflection: - Laser spot is focused near $1/4^{\text{th}}$ of the length of the beam that provides maximum angular deflection. This angular deflection depends on vertical deflection of the beam. Since a fixed-fixed beam structure provides more angular deflection than a cantilever beam, for the same vertical deflection, the resolution is improved. Also, the displacement is interpreted in term of A-B voltage on PD as explained in section 2.2.1, higher displacements are also beneficial from data acquisition point of view because it reduces the noise of A-B signal. Thus we can get clearer and more accurate A-B data plots *i.e.* force signal with high resolution from a fixed-fixed beam than that in cantilever beam. We have used three types of force sensors having doubly fixed beam structure. Following table, Table 2.1 gives the specifications of these force sensors.

Beam Type	Length (μm)	Width (μm)	Thickness (μm)	Resolution (μN)
Short	90	20	4.5	2.3
Long	120	20	4.5	1.2
Long-slim	200	15	4.5	0.3

Table 2.1 Specifications of the Force Sensors

The short beams were mostly used for conducting high-force measurement tests ($\geq 500 \mu\text{N}$) while long beams were used during low force measurement tests ($\sim 100 \mu\text{N}$). Only a few tests were carried with long-slim beams at very low forces ($\leq 25 \mu\text{N}$).

2.3 Mechanical Set-Up

The mechanical set-up consists of three modules

1. Vacuum system
2. Lifting system
3. N_2 flow assembly for ambient control

2.3.1 Vacuum System and Plasma Source Generator: -

The main purpose of building the vacuum system is to generate plasma of different gasses. It can also help in ambient control for doing *in-situ* testing. The plasma source generator used in this system is Astron AX7670 by MKS because of its ability to handle different gasses. It is easy to ignite by applying 24V and also has gas flow interlock and thermal switch inbuilt. Any unwanted temperature rise due to the lack of cooling water supply or any out-of-range pressure variation

can turn off the plasma generator. The vacuum system is designed according to the pressure and flow requirements for the plasma generator. It has following components

- Chamber: - The vacuum chamber is made of stainless steel and it has different ports for connecting vacuum hose, UV lamp (HAMAMATSU L2D2 L7202), pressure gauge, electrical feed-throughs and an extra port. The detailed drawing is given in Appendix C. A rubber O-ring is provided at the bottom for tight sealing.
- Vacuum pump: - The vacuum pump used in this system is 'IDP-3 Dry Scroll Pump' from Varian Inc. Its compact and oil-free working feature is mainly suitable for our application. Any presence of oil particles inside the vacuum chamber can undergo unwanted chemical reaction in the presence of oxygen plasma and severely contaminate the samples. The pumping speed of 60 liters/ min is sufficient for our application and low noise and vibration gives is beneficial while doing *in-situ* plasma cleaning experiments.
- Vacuum hose: - This is a total 9' long and stainless steel hose having $\frac{3}{4}$ " as outer diameter that connects the pump to the vacuum chamber. Three 3' long hoses are connected to each other with KF16 flanges. This allows us to install the valves in between the pump and vacuum chamber. The total length of the hose is selected by considering the distance of the AFM from the nearest available location of the pump. However the diameter is designed according to the pressure and flow requirements of the plasma generator. Calculations are shown in Appendix B.
- Needle valve and main valve: - Main valve is connected in between the needle valve and pump. Its function is to connect or disconnect the vacuum pump to the chamber when required. Needle valve is installed for regulating air flow rate going into the pump at specified. It is opened while main valve is closed before turning on the pump and closed

when the main valve is opened for creating vacuum inside the chamber. If the pump is kept running for longer with the main valve closed without using a needle valve then high vacuum gets created in the vacuum hose. This can cause the oil from the pump to enter into the vacuum hoses Flow controller for controlling gas-flow for the plasma generator. The needle valve installed here is an ‘Edwards Needle Valve’ from Kurt J. Lesker Company having maximum flow rate of 0.1 lps (@ 1bar diff.)

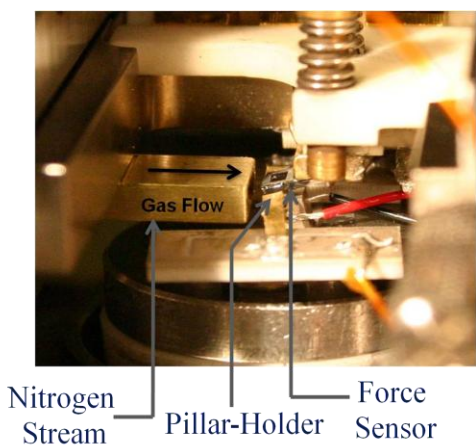
- Flow controller: - Three Smart Trek Series 100 mass flow controllers are located for three gasses namely Ar, O₂ and NF₃ respectively. These are software controlled and accurately regulate the corresponding gas flows with the resolution of 0.005 lpm.
- Tubes for connecting gas tanks to the controller and plasma source: - The tubes are 9' long and 0.25" in diameter made of stainless steel. These are bent to form spiral shapes for reducing stress and connected to the flow controller with ¼" VCR fittings. The gasses are mixed after passing through the controller and fed to the plasma source by one single ¼" stainless steel tubing connected with the help of VCR fittings.
- Water cooling system: - A minimum of 1.5 gpm water-flow is necessary for plasma generator. A standard 1' long AP11T filter is installed before letting the water into plasma chamber. Simple 5/8" PVC tubing with Swagelok fitting is utilized for this purpose.

2.3.2 Lifting System: -

The lifting system is quite simple. An aluminum stand is connected at the back of AFM with the help of screws and aluminum blocks. It supports total four pulleys, one at the top, two in center and one at the bottom as shown in diagram. These pulleys guide the metal-rope that connects electric winch to the plasma generator and vacuum chamber. Electric winch is specifically

selected because of its slow operating speed of 3.5 fpm and 2700 lbs lifting capacity. Since the total weight of plasma generator and chamber is below 100 lbs, no critical calculations were required for selecting the pulley or motor of the winch. Only the upper pulley actually carries the total load while all the other three act as guiding pulleys. Stainless steel bearing pulleys are selected for their oil free operation and higher load carrying capacity. Detailed drawing is given in Appendix 4.

2.3.3 Nitrogen Flow Assembly for Ambient Control:-

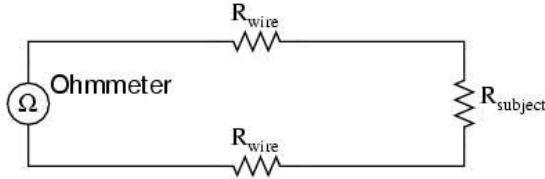


Ambient control is another important feature of this set-up. Lack of ambient control develops significant amount of contamination at the contact spots especially for the refractory metals like Ru, Ir etc. Laminar flow is required to minimize the concentration of contaminants near the contacts. GP240 liquid nitrogen tank is used since it stores

Figure 2.5 Nitrogen-Ambient Control

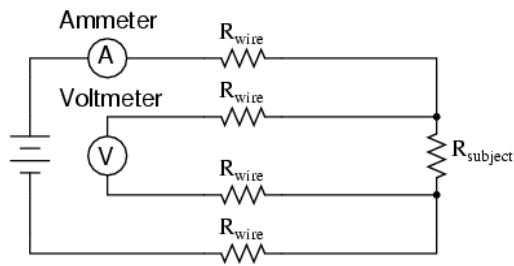
99.99% of pure nitrogen. Swagelok fittings are used for connecting $\frac{1}{4}$ " stainless steel pipe to the flow controller that controls nitrogen flow at 0.9 lpm. After the flow controller, combination of stainless steel and brass tube is used to carry the nitrogen near the contact spots as shown in figure 2.5. The final tube that actually focuses nitrogen stream over the samples has rectangular cross section of $3/16"$ x $3/32"$. It is fixed inside the AFM with the help of an aluminum holder. Different components such as tube holders and adapters for tube fittings were designed by using Pro-E. Calculations for gas flow and drawing of the holder are provided in Appendix A and Appendix E respectively.

2.4 Electrical Set-Up



Ohmmeter indicates $R_{\text{wire}} + R_{\text{subject}} + R_{\text{wire}}$

Figure 2.6 Two-Wire Resistance Measurement



$$R_{\text{subject}} = \frac{\text{Voltmeter indication}}{\text{Ammeter indication}}$$

Figure 2.7 Four-Wire Resistance Measurement

The challenging task of any micro-contact test set-up is to accurately measure the actual resistance across the contact. A simpler way of measuring contact resistance is to use two-wire resistance measurement method and then subtract the approximated resistance induced from wires and connectors from the measured resistance to get estimated contact resistance. Even though this method can reasonably estimate the contact-data, it is still not accurate and consists of lots of errors. The efficient way of acquiring accurate contact resistance measurement is to implement four-wire-resistance. Following section explains the theory of using four-wire resistance measurement instead of two-wire.

As shown in the Figure 2.6, an Ohm-meter directly used to measure the contact resistance includes resistances from connecting wires and connectors leading to erroneous data. R_{wire} represents the resistance induced from the connecting wires. Usually the wires are small and R_{wire} is also small (few ohm per 100 feet depending on the wire-cross-section)(25) but since it is required to measure the resistances in the range of milliohms for quantitatively comparing different materials for their reliability and life time, this method is undesirable. Two-wire resistance measurement is usually recommended when the resistance to be measured is in the

range of few hundreds of ohms. In that case the error gets minimized since wire resistance becomes small as compared to $R_{measured}$. In four-wire resistance measurement (figure2.7) current is sourced through the circuit and voltage drop is measured across the subject i.e. micro-contact instead of directly using an ohmmeter. The current flowing from the entire circuit remains the same while the potential drop is obtained directly across the subject. The voltmeter wires carry very small current so the long lengths of wires connecting the voltmeter across the $R_{measured}$ will drop negligible amount of voltage. Thus the voltage indicated by the voltmeter is almost equal to the actual potential drop across the contact leading to accuracy in measurement. Contact resistance is then simply given by Ohm's law that is stated as

$$R_{measured} = \frac{V_{measured}}{I_{measured}}$$

As shown in Figure 2.8, the actual set-up consists of a V_R , a 22Ω resistor *i.e.* R in series with the

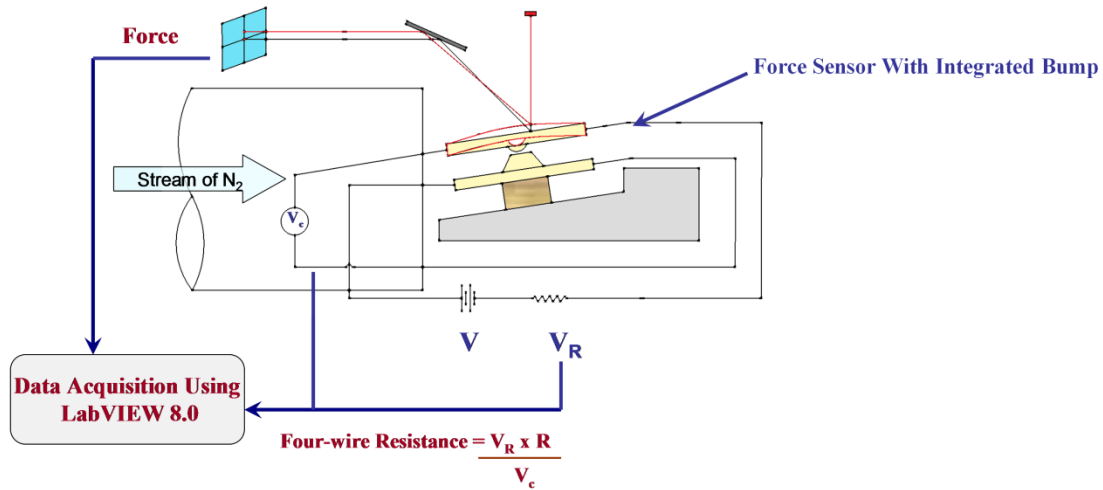


Figure 2.8 Electrical Set-Up

voltage source. Constant voltage is biased from the voltage source. As the current, $I_{contact}$, flows from the contact resistance as well as the 22Ω resistor, the circuit acts as voltage divider that gives us $R_{contact}$ as

$$I_{contact} = \frac{V_{resistor}}{R (22\Omega)} - \frac{V_{Contact}}{R_{contact}} \quad i.e. \quad R_{contact} = \frac{V_{contact}*22}{V_{resistor}}$$

Two voltage drops across the 22Ω resistor ($V_{resistor}$) and contact resistance ($V_{contact}$), are recorded by the LabVIEW program. For doing the cold switching tests it is required that voltage should be biased only after the contact is made. However, if applied continuously then it should be below 400 millivolts (4) for avoiding contact-damage due to hot switching and snap-in contact.

Set-Up for Piezo

The force sensor and pillar used during all of the experiments imitate the upper and lower portion of an actual switch. However in our system the switching action between contact bump and pillar is achieved with the help of piezo-electric material. We have used PL022.31 from PI. It is attached to a stainless steel disc having a groove of 12^0 angle and 2mm wide with the help of thermoplastic material STAYSTICK 442. This angle is corresponding to the default 12^0 angle of the AFM tip-holder. It is done by keeping the thermoplastic in between the piezoelectric material and the disc. The entire stack is placed on a hotplate at 100^0 C. The thermoplastic melts and piezo gets glued to the disc when it is cooled down. The pillar should always be stable on this piezo with two connections provided on the bottom side for four-wire resistance measurement as shown in figure 2.8. For serving this dual purpose metallic spring like structures are welded on the custom built Alumina substrate. For electrical connections two palladium silver pads are provided on it.

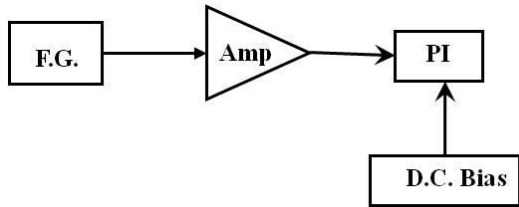


Figure 2.9 Schematic Diagram Showing Piezo Set-Up

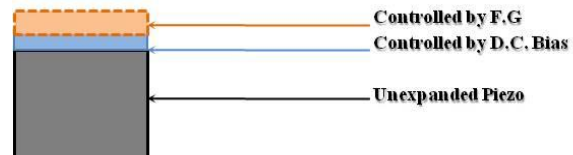


Figure 2.10 Piezo Expansion Model

FG: - Function Generator from Agilent

Amp: - Custom Built Amplifier

PI: - PL022.31 piezo from PR

DC Bias: - Source Power Supply from Agilent

The piezo is actuated by the ramp function. It is loaded in first 5 milliseconds and unloaded in 5 milliseconds. When operated at 1 Hz, the remaining time is utilized in data acquisition. Agilent function generator is used for this purpose. The signal is fed to the amplifier having gain of ~8.25. The amplified signal is then used for actuating the piezo. In addition to the function generator, the piezo is also actuated by a DC power supply as shown in figure 2.9. This DC bias always keeps the piezo in expanded position (figure 2.10). The amount of expansion being dependant on the bias voltage applied, DC biasing gives added control while engaging the tip using AFM. This voltage is especially effective while keeping the force constant. While doing the cycling tests at higher frequencies (800Hz), the piezo experiences a small drift that reduces the force on the beam. In this situation DC bias on the piezo is increased to keep the force constant. It is recommended to keep it ~ 30 V at the beginning of the cycling tests however it varies as the cycling continues depending on piezo drift. The piezo is constructed in small stacks. When it is new, it gives full expansion of 2.2 μm at 100 V. Since the maximum range of voltage for operating the piezo is piezo is -20V to 100 V, it is recommended that total voltage used for expanding the piezo should be kept as low as possible for extending its life. For e.g. amplitude of 8 V from function generator and D.C bias of 20 V drives the piezo at ~86 V for achieving the expansion of ~1.9 μm . While doing cycling tests at higher frequencies (~100Hz) such a high

voltage can damage the piezo layers one by one and reduce its expandability. Reduction in piezo-expandability can make it unable to be used for performing high-force-measurement tests (≥ 500 N μ). Typically in our experiments a beam with 120 μ m of length would require 0.2 μ m of vertical displacement for loading the micro-bump at 500 μ N that can be achieved by applying 10V to the piezo after making contact. However we have to keep some space (~ 200 nm to 300 nm) between the bump and pillar for ensuring proper separation after unloading in the case of larger pull-off forces. We also need to keep some room on DC- bias for encountering the piezo drift. This makes the total driving voltage of ~ 40 V for a perfectly working piezo. However with damage of piezo-layers over the period of time, the expansion decreases. Such a situation requires higher voltages for achieving required forces.

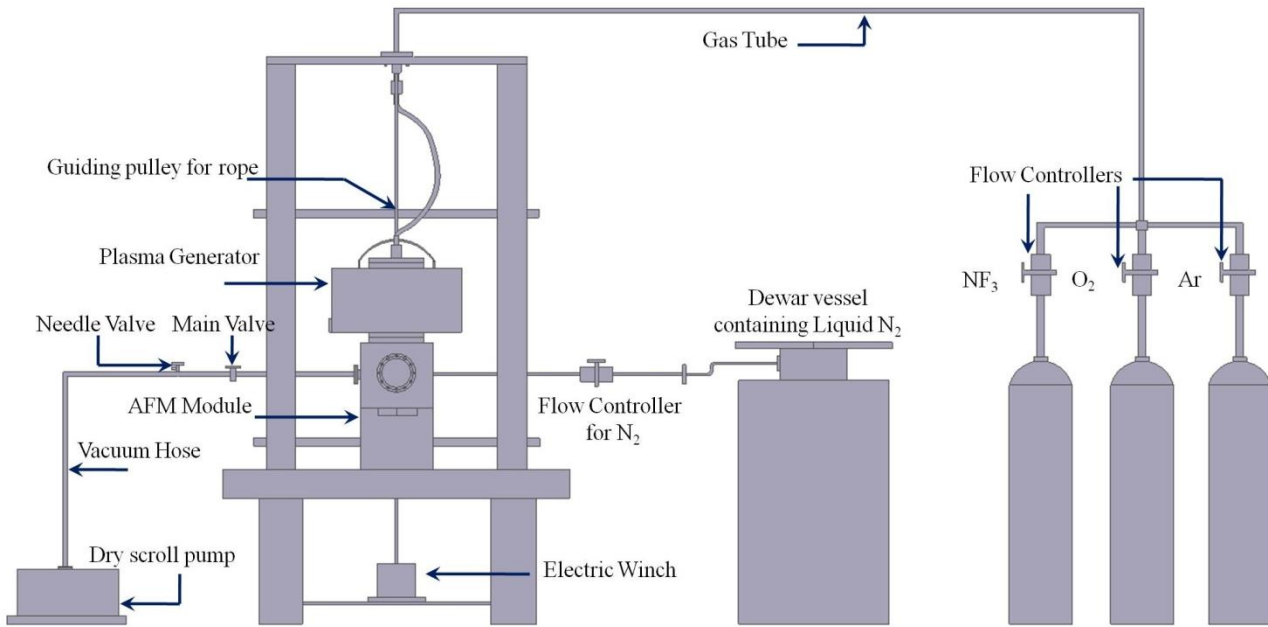


Figure 2.11 Schematic Diagram Showing Entire Set-Up

2.5 Testing Procedure

For conducting contact evolution study we require the force and resistance data across contact. This data is not directly acquired in this set-up but in the form of three signals *i.e.* 1) A-B signal from PD of AFM 2) Voltage drop across contact and 3) Voltage drop across $22\ \Omega$ resistor. Previous section described how the two voltages and resistor interpret the contact resistance. The A-B signal in reality gives the voltage reading on the PD depending on the laser beam deflection. In order to convert this voltage signal into the force two types of calibrations are required.

- 1) **Calibration of z-piezo of AFM:** - The JEOL SPM has its own piezo that accurately

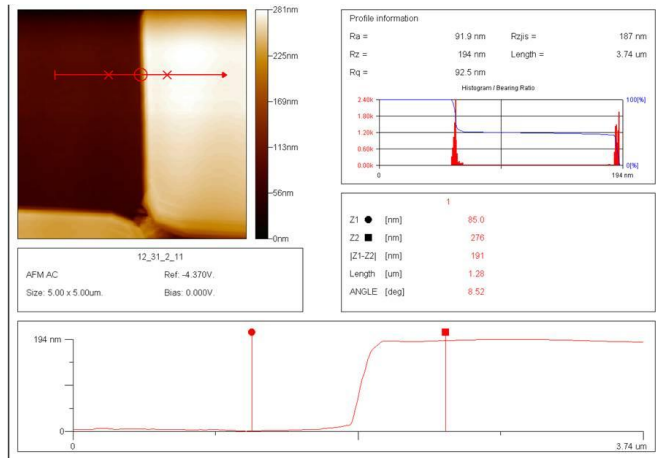


Figure 2.12 AFM Image of the Calibration Sample

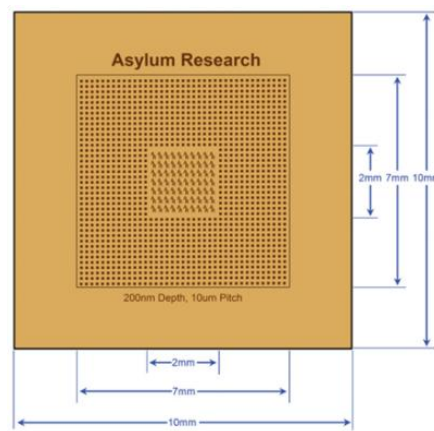


Figure 2.13 Calibration Sample

controls the vertical motion of the tip at nanometer level while performing scanning also called as z-piezo. It is done by the electronics inside the AFM by regulating the voltage on it. The Z-piezo calibration tunes the voltage needed for applying certain piezo displacement. This is further required for doing Force vs Displacement test while doing force calibration. Regular AFM cantilever is scanned in AC Mode across the calibration sample 900.238 from Asylum Research having step height of 200 ± 20 nm. Figure 2.13 shows the calibration sample and the results after scanning is shown in figure 2.12. Since,

the step height shown by AFM *i.e* 191 nm is well within the tolerance limit of the sample, no changes in calibration scale were required.

2) **Force Calibration:** - This calibration actually interprets the A-B voltage signal in terms of displacement in nanometers. While performing this, some finite displacement say 100nm is given to the regular AFM tip by executing Force vs Displacement function in AFM. The AFM displays voltage vs displacement curve that helps us interpret the A-B voltage in terms of displacement. It was found to be 33nm per volt which is further multiplied by the stiffness 'K' of our doubly fixed beams. Thus the same A-B voltage difference *i.e.* displacement can be used for applying different force by using beams of different dimensions. It is easier to vary the length from microfabrication point of view. So, the shorter beam can be used for conducting tests at higher forces because of their higher stiffness and vice versa (displacement being constant). For doubly fixed beams loaded at center, stiffness is given as (4).

$$K = \left[\frac{192 \cdot E \cdot I}{L^3} \right] \text{ Where,}$$

E = Modulus of elasticity of Si, typically 150N/m to 180 N/m

L = Beam-length, varies from $\sim 90 \mu\text{m}$ to $200\mu\text{m}$

I = Area Moment of inertia of the beam

For a rectangular cross-section $I = \frac{w \cdot t^3}{12}$

t = Beam-thickness, typically $4\mu\text{m}$ in our case

w = Beam-width, typically $\sim 20 \mu\text{m}$ in our case

Hence,

$$K = 16 E \cdot w \cdot \left[\frac{t}{L} \right]^3$$

2.5.1 Procedure for Testing

Before starting the actual measurement of contact resistance, it is necessary to secure both the chips of pillar and force sensor firmly on the respective holders. Since tweezers are used to hold the Si chips and mounting them on the holders, care should be taken not to scratch them from sideways. Even a small scratch can bring significant number of particles on the surface and pose problems during contact engagement. For avoiding contamination problems due to skin oil it is always recommended to wear gloves all the time during experimentation. Also, direct breathing over the samples while mounting them on the holders is not advisable due to the contamination issue. After setting up the sample on the corresponding holders continuity check should be performed to see if the springs are making proper contact with the metallic layer of the samples. Lack of proper contact of the springs to the samples can measure either no or very high contact resistances. Perform following steps for contact resistance measurement after aforementioned care is taken.

Steps

- 1) Focus laser spot on the right paddles so that there is no obstruction in laser-path.
- 2) Set the AFM in contact mode and reference at -1.8 V to -1.6 V. Accurately adjust PD position so that voltage at reference is exactly -2 V.
- 3) Turn off laser and start the coarse adjustment by using the screw for Z+ movement.
- 4) Observe for the image clarity of force sensor and pillar by adjusting focal length of the camera.
- 5) When the force sensor and top of the pillar are approximately at same focal length, stop coarse movement.
- 6) Accurately locate center of the beam over pillar.

- 7) Turn the laser on and check PD again.
- 8) Click on ‘retract off’ and then ‘approach on’ to put the AFM in feedback mode while approaching. Wait for a while until you hear a beep.
- 9) The beep indicates that the laser beam has moved from set position to the reference position i.e. the bump is in contact with the pillar. Observe the laser spot deflection.
- 10) If it is not vertical then retract the sample and move out. Lateral movement of the laser spot can be an indication of improper contact causing slight twisting of the beam.
- 11) If it is vertical (retract on and retract off and check contact-current) then apply 35 V DC bias voltage to the piezo.
- 12) Go to the ‘advanced’ mode in AFM to turn off the feedback mode. Come back to contact mode and observe the laser spot by clicking on ‘adjust PD’.
- 13) Reduce bias and observe the laser spot on PD. It will try to come back from the reference position (-1.8 V to -1.6 V) to -2 V which is standard position of a freestanding tip. When PD voltage is -2 V, apply 0.2 V across the contact and look at the current. Current should be zero.
- 14) Apply waveform by using function generator.
- 15) Slowly increase amplitude of the waveform for increasing piezo displacement until required ΔV is reached.
- 16) Acquire the data by using the LabVIEW software as soon as possible to limit the initial data collection below 10 cycles.
- 17) Follow cycle-frequency table (Table 2.1) while performing cycling tests.
- 18) Important points to remember

- a. Try to locate the contact accurately before coarse adjustment to avoid greater X and Y movements
- b. Constantly observe contact spots during coarse adjustment
- c. Observe for the drift during feedback mode and monitor -2 V on PD
- d. Try to keep pillar as close to bump as possible and avoid higher voltage on piezo for more piezo life and reducing optical interference.
- e. Constantly monitor piezo drift during cycling and increase or lower the bias voltage or amplitude to keep ΔV constant. Do not apply more than ~8 V to piezo.

Redo the engagement and follow the same procedure again

2.5.2 Procedure for Plasma Cleaning

Clean the chamber before cleaning the first sample. We have followed the standard procedure for cleaning the chamber *i.e.* 3 min of Ar plasma + 3 min of O₂ plasma +3 min of Ar plasma. Initial phase of Ar plasma cleaning is applied just to start the system. The time span of 3 min gives the system enough time to stabilize. Also 3 min of Ar plasma treatment at the end is used in order to remove most of the contaminants that could have formed during O₂ plasma cleaning phase. Reduction of this time span to lesser than 3 min does not make any significant changes as far as cleaning is concerned. Follow the steps as mentioned below for plasma cleaning.

- 1) Turn on cooling water supply all the tanks and main power supply.
- 2) Check that main valve is closed and needle valve is open.
- 3) Start the pump.
- 4) Slowly open the main valve and turn off the needle valve for applying the entire pump pressure at the vacuum chamber.

- 5) Observe for the drop in pressure indicated by pressure sensor.
- 6) At around 150 to 200 mTorr, turn on Ar supply at 0.3 lpm.
- 7) Observe for ‘Ready’ signal at plasma indicator.
- 8) When it’s stable at around 1750 mTorr turn on power to switch on plasma.
- 9) After three minutes start 0.15 lpm of O₂. Wait and observe for color/brightness and pressure change.
- 10) Brightness will suddenly increase when O₂ plasma starts
- 11) Slowly ramp up the O₂ supply to 0.5 lpm in the steps of 0.05 lpm
- 12) Wait for 3 min and then turn off O₂ supply.
- 13) Keep Ar plasma on for 3 min.
- 14) Turn off the supply.
- 15) Turn off the main valve and open the needle valve and monitor pressure rise in the chamber. Increase Ar flow rate to bring the chamber back to atmospheric pressure quickly.

For sample-cleaning follow the same steps with 3 minutes of Ar followed by 10 minutes of O₂ plasma cleaning

Table 2.2 is the cycle-frequency table used while doing cycling. It should be noted that the contacts are cycled at corresponding frequencies as mentioned in table but after each cycle it is reduced to 1Hz for data acquisition. The ‘Cycles’ column shows the total number of cycles performed until we reach to a particular row while the figures inside the bracket ‘()’ represents the number of cycles that are performed in that particular step corresponding to the ‘Frequency’ and ‘Time’.

No.	Cycles	Frequency	Time
		Hz	
1	10	1	10sec
2	50(40)	1	40 sec
3	100(50)	1	50 sec
4	500(400)	10	40 sec
5	1000(500)	10	50 sec
6	2000(1000)	20	50 sec
7	5000(3000)	60	50 sec
8	1e4(5000)	100	50 sec
9	2e4(1e4)	100	1m40sec
10	5e4(3e4)	300	1m40sec
11	1e5(5e4)	500	1m40sec
12	3e5(2e5)	800	4m10sec
13	5e5(2e5)	800	4m10sec
14	7e5(2e5)	800	4m10sec
15	1e6(3e5)	800	6m20sec

Table 2.1: - Cycle-Frequency Table

Chapter 3- Simulation

3.1 Simulation of Pure Au-Au Contact

According to the formula given by Holm (26), the constriction resistance is given by

$$R_H = \frac{\rho}{2a} \quad \text{--- (1)}$$

where ρ is the resistivity of the contacting metals and 'a' is the radius of circular contacting spot.

This formula holds good for the contact-spots connecting semi-infinite bodies. In MEMS switches surfaces are often coated with the films having varying thicknesses (from $\sim 10\text{nm}$ to $\sim 1\mu\text{m}$). As a contact-bump starts making contact with its counterpart, the nano-asperities present on the films start getting pressed against each other. Increase of force brings more and more asperities into contact resulting in increase of effective contact area. The total contact area is, thus, few hundred times smaller than the contact bump or bottom part. In cases, when the contact area is no longer small as compared to the thickness of the film, application of equation (1) for estimating constriction resistance by Holm's theory can consist of some errors. It is called as distorted constriction (9). The contact resistance is no longer dominated by the Holm constriction at the contact. In this case we need to include the spreading resistance from the contact area into the thin film.

According to the simulation performed by Eid (27), the radius of Au-contact, ‘a’, is $\sim 0.34\mu\text{m}$ with the film thickness of 300 nm when the contact is loaded at 500 μN . The force sensor is $\sim 20\mu\text{m}$ wide and $\sim 80\mu\text{m}$ long. In this case ‘a’ becomes comparable to the film thickness and contact resistance predicted by Holm is 0.0717Ω if we consider $\rho = 2.44\mu\Omega\cdot\text{cm}$ for Au (28). Most of

the measured values have always remained considerably higher ($\sim 0.15 \Omega$ to $\sim 0.18 \Omega$) than predicted by the theory.

The simulation for pure Au-contact is conducted to understand the trend of resistance when the thickness of the film is varied. This simulation also helped us in closely predicting the contact resistance values for particular metallization stack when loaded at particular force. The simulation mentioned in the next sections of this chapter were performed by me under the supervision of Dr. Chen.

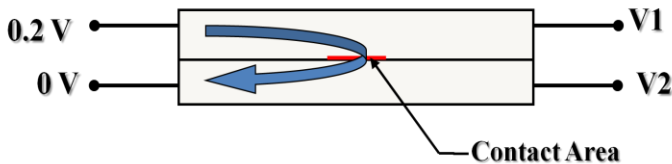


Figure 3.1 Schematic Diagram of the Model of Simple Metal-Metal Contact

For conducting the simulation electric module Ansys 11.0 is used. For performing current conduction analysis ‘SOLID 98’ element is selected. It is a tetrahedral element with 10 nodes. It can

take 6 degrees of freedom. According to Ansys reference manual, (29) for conducting steady state current conduction analysis only current and voltage DOF are applied and the output is given in the form of current density and voltage distribution. Ansys sparse solver which is the default solver is used for conducting the simulations.

In first model the contact radius is kept constant at 0.5 μm and two block of 40 $\mu\text{m} \times 40\mu\text{m}$ are connected to each other only at this contact area as shown in figure 3.2 and the third dimension *i.e.* thickness is varied. Since the entire testing is done by conducting four-wire resistance measurements, similar conditions are taken while doing simulations as well. Voltages of 0.2V and 0 V are applied at the corresponding areas as shown in figure 3.1. All the other areas including the area surrounding the contact area are insulated. For this simulation bulk resistivity

of Au is taken as $\rho = 2.44\mu\Omega\text{-cm}$ (28) and

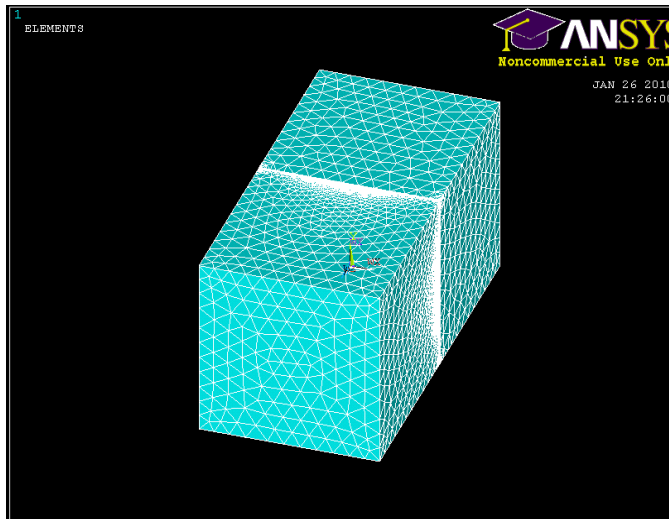


Figure 3.2 Meshing of Two 40 $\mu\text{m} \times 40\mu\text{m}$ Blocks in Contact With Each Other By Contact Area Having $a = 0.5\mu\text{m}$ Radius

the height of the contact area is zero. This voltage difference drives the current through the contact area as shown by the blue arrow in figure 3.1. Both these volumes are meshed at fine level (Fine 1) by using Ansys smart meshing tool and type of elements used is tetrahedral. For improving the accuracy of the results the areas near the contact-area are refined at the

level of refinement of 1 as represented in figure 3.2. Thickness of the two blocks is decreased from 40 μm to 0.1 μm in 9 steps. Decrease in thickness from 40 μm to 100nm causes a large change in aspect ratio. This variation also causes a large increase in the total number of elements formed in the model after meshing. In every step the voltage drops on the opposite areas are observed as they are measured as V1 and V2 respectively. ($V_1 - V_2$) gives the total voltage drop across the contact. Current flowing through the contact area is same as the one flowing from the area where 0.2 V is applied. Current density recorded by the Ansys postprocessor is multiplied

by this area to get current flowing from contact. Contact resistance, R , is then calculated by using Ohm's law.

$$R = \frac{(V_1 - V_2)}{I} \quad \dots \dots \dots \quad (2)$$

Figure 3.3 illustrates the simulation results of this model. Ansys simulation results agree well with the Holm's model when the thicknesses of blocks are larger as compared to the contact-diameter. However as when the block-thickness becomes comparable to the contact-diameter, the simulated resistance remains no longer consistent with Holm's theory. So, a 300 nm thick Au-Au contact having 0.5 μm contact radius would have the four-wire resistance in the range of 0.8 Ω instead of 0.024 Ω as predicted by Holm's theory.

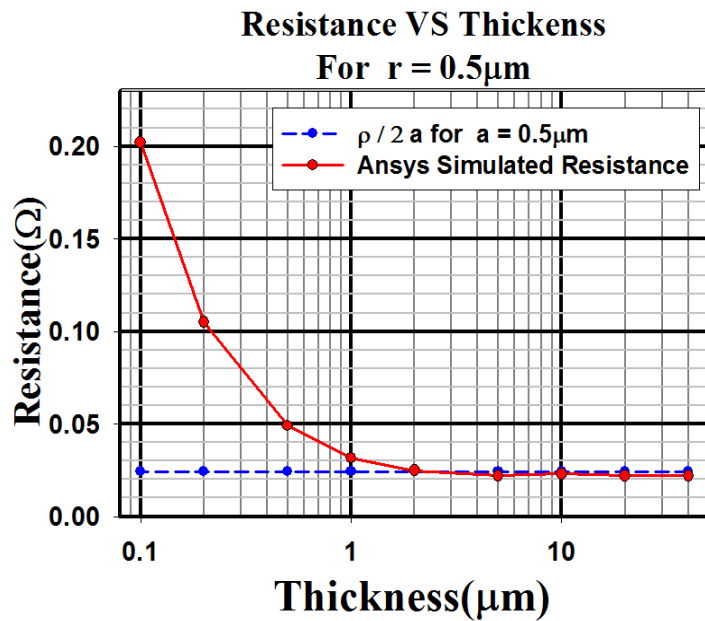


Figure 3.3 Simulation Results Showing Resistance vs Thickness Plot

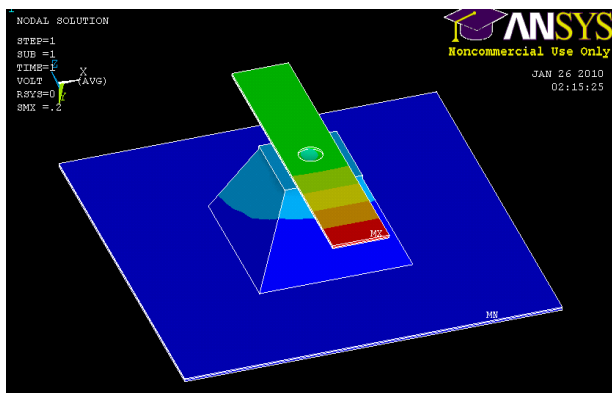


Figure 3.4 Simulated Voltage-Distribution for the Model With Real Geometry

by modeling the contact-radii at corresponding forces (Table 3.1) for corresponding metals. The models are created in Pro/ENGINEER WILDFIRE 4.0. Figure 3.4 shows an example of voltage distribution for Au-Au contact loaded at 500 μ N. Resistivity of 300nm film was measured as 3.6 $\mu\Omega\text{-cm}$ for Au and 13.8 $\mu\Omega\text{-cm}$ for Ru. The force sensor modeled here is 15 μm x 80 μm and 4 μm thick. It has a contact bump having radius of curvature of 20 μm and 1 μm height. The pillar is having trapezoidal shape with the bottom-square of 40 μm and top-square of 20 μm . Height of the pillar is taken as 20 μm and the substrate is 100 μm X 100 μm . Table 3.1 given below gives contact resistances for these structures at respective forces and compares it with the values estimated by equation (1) and experimentally measured data. Experimentally measured values show close resemblance with the values predicted by Ansys models especially at 500 μN . This can be because of the involvement of spreading resistance at higher forces due to higher contact radii. Another reason behind this close agreement between measured values and Ansys-predicted values can be due to the sheet resistance of thin metallic films on the pillar walls.

The simulation is further pursued by modeling the real structures coated with 300 nm of Au and Ru respectively. Contact radii are taken from the simulation performed by (27). Since most of the metal-contact pairs are tested at either 100 μN or 500 μN during the experiments, simulations are conducted

Applied Force	Au				Ru			
	Contact Radius (μm)	R (Ω)	Measured R (Ω)	$\frac{\rho}{2a}$	Contact Radius (μm)	R (Ω)	Measured R (Ω)	$\frac{\rho}{2a}$
500 μN	0.341	0.09	0.14	0.053	0.187	0.63	0.65	0.37
100 μN	0.2 μm	0.13	0.203	0.09	0.124	0.702	0.8	0.56

Table 3.1 Simulated Contact Resistances for the Model With Real Geometry

3.2 Simulation of Layered Ru

Layered Ru is a new kind of contact-metal that is studied during experimentation. This comprises of Ru-layers having thicknesses of 10 nm, 50 nm, 100 nm, 300 nm deposited over 300

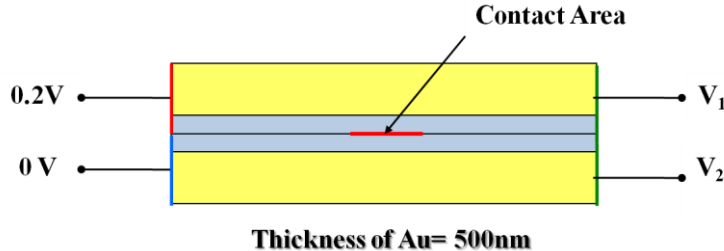


Figure 3.5 Schematic Diagram of the Model Having Layered Structure

nm layer of Au respectively over the Si force sensor. The pillars are initially electroplated with Au having the thickness of 500 nm for avoiding the sheet resistance effect arising from pillar-walls. It is further sputter-coated

with 300 nm of Au layer. Hence, the total Au thickness for pillar becomes 800 nm. The advantage of using Au layer beneath the Ru is that the lower resistivity of Au allows most of the current to pass through the Au layer when the Ru-Ru contact is made. It is further explained in detail in Chapter 4.

The model used here is quite similar to the one used in previous section however it consists of two layers on one side of the contact as shown in figure 3.5. The thickness of Au layer is fixed at

500 nm for simulation while the Ru-layer thickness varies in each set. The contact-radii at different forces where Ru-layer from one component meets the Ru-layer of the other is selected from (27). Total four sets of Ru thicknesses *i.e.* 10nm, 50 nm, 100 nm, 300 nm over 500 nm of Au are simulated. *Figure 3.6* shows the increase in contact-radius with the increase in applied force. All the parameters used in this simulation are similar those in previous section. Bulk resistivity of Au is taken as 3.6 $\mu\Omega\text{-cm}$ from experimentally measured data. *Table 3.2* gives the resistivity values of Ru films. These values are measured experimentally and used for doing simulations.

No.	Thickness (nm)	Resistivity ($\mu\Omega\text{-cm}$)
1	300	14.82
2	100	21.34
3	50	25.89
4	10	36.4

Table 3.2 Measured Resistivity Values for Different Thicknesses

In this case, the total contact resistance is approximated as the sum of constriction resistance R_c and film resistance R_f (9) It is represented as

$$R_{CR} = R_c + R_f = \frac{\rho}{2a} + \frac{\rho' d}{\pi a^2}$$

Where ρ' is the resistivity of Ru film and ρ is the resistivity of the bulk material which is Au in our case.

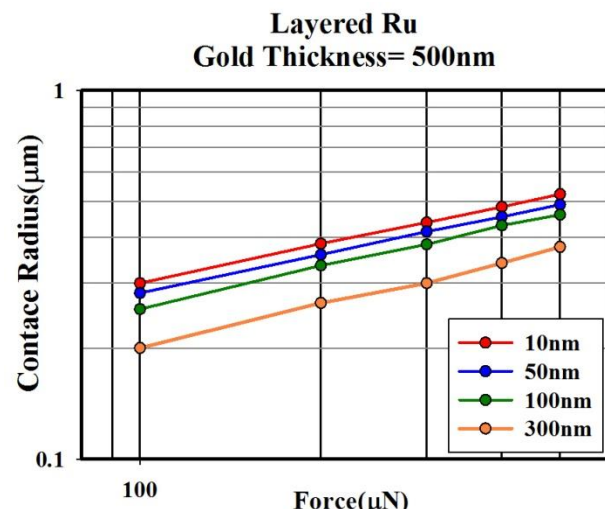


Figure 3.6 Simulated Contact Radius vs Force by Eid(27)

Since the thickness of 50 nm and 10 nm Ru films becomes comparable to the mean free path of electrons flowing from Au and Ru layers, Sharvin resistance has to be taken into consideration. The electrons flowing across the cross-section also suffers extra resistance at the boundary separating two metals called as boundary scattering.

If the constriction resistance is accurately calculated by considering the both these effects into account then R_{CR} can be given as

$$R_c = \gamma \frac{\lambda}{a} R_M + R_s = \frac{1+0.83(\lambda/a)}{1+1.33(\lambda/a)} \cdot \frac{\rho}{2a} + \frac{4\rho\lambda}{3\pi a^2}$$

$$R_{CR} = \gamma \frac{\lambda}{a} R_M + R_s = \frac{1+0.83(\lambda/a)}{1+1.33(\lambda/a)} \cdot \frac{\rho}{2a} + \frac{4\rho\lambda}{3\pi a^2} + R_f \quad \dots \quad (3)$$

Where R_M is the Maxwell spreading resistance due to lattice scattering and R_s is the Sharvin resistance due to the boundary scattering (9). Furthermore ρ is the electrical resistivity of Ru, γ is the interpolation function and λ is the mean free path of electrons *i.e.* 10.8nm for Ru and 38nm for Au.

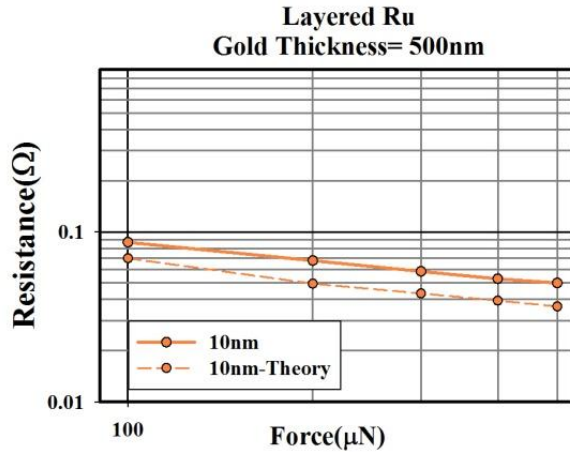


Figure 3.7 Simulated Contact Resistance vs Force for 10nm Ru Layered Over 500 nm Au and Model Represented by Equation (3)

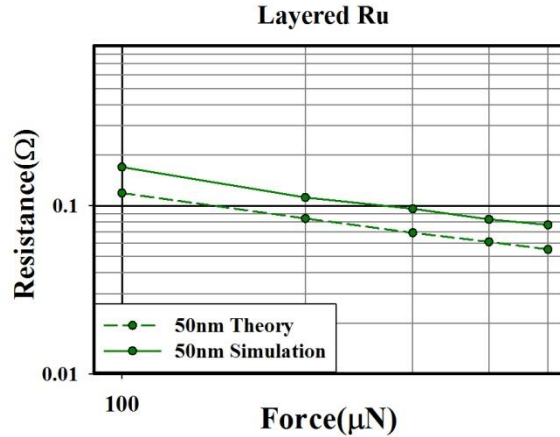


Figure 3.8 Simulated Contact Resistance vs Force for 50nm Ru Layered Over 500nm Au and Model Represented by Equation (3)

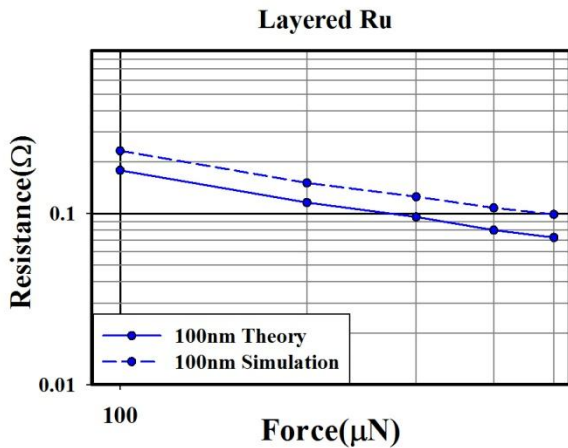


Figure 3.9 Simulated Contact Resistance vs Force for 100nm Ru Layered Over 500nm Au and Model Represented by Equation (3)

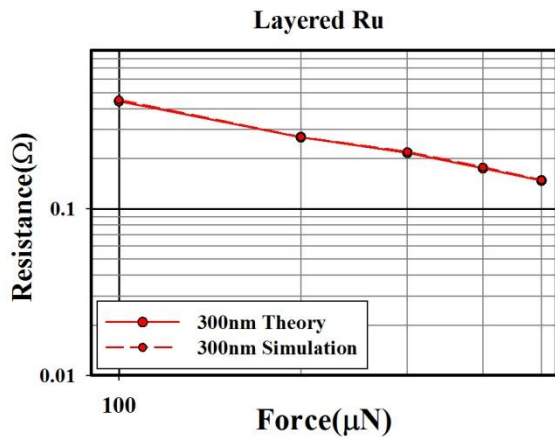


Figure 3.10 Simulated Contact Resistance vs Force for 300nm Ru Layered Over 500nm Au and Model Represented by Equation (3)

Figures, from 3.7 to 3.10, show the comparison between the contact resistance simulated by Ansys with the one predicted by theory for four Ru thicknesses *i.e.* 10 nm, 50 nm, 100 nm and 300 nm, over 500 nm Au. In three cases of Ru thicknesses namely 10 nm, 50 nm and 100 nm, the theory underestimates the contact resistance, as compared to simulation by very small value which can be due to the different assumptions made in the equation (3) given by (9). It can also be due to the difference in spreading resistance effect estimated by Ansys as compared to

equation (3). For 300nm layered Ru case, the model given by equation (3) seems to agree well with the Ansys model. This can be due to the contribution of resistances from thick Ru films. At 300 nm Ru films have smaller contact radii as compared to the Ru thickness especially in low force regime ($<500 \mu\text{N}$) . In this case Ru can behave like bulk material instead of a film.

Chapter4- Discussion of Data and Results

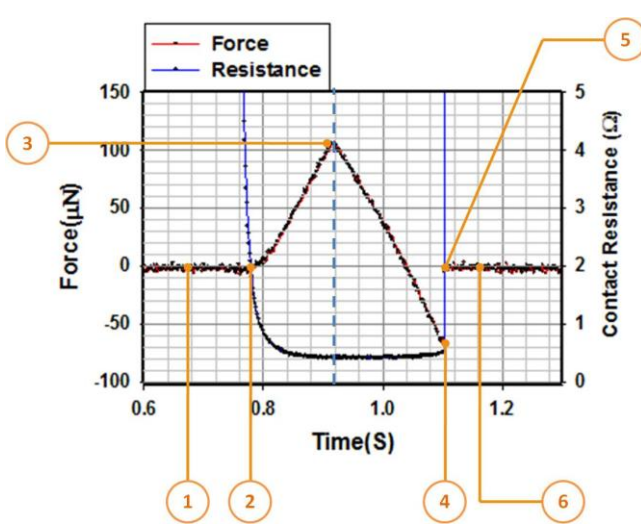
4.1 Au_Au: -

We started our experiments with Au on both sides of the contact. As we have seen in Chapter 1 that Au is a popular metal in MEMS contact switches, several attempts have been made to test it in different conditions. As we will see in next section, most of the research groups have reported stiction problems. Gold, with its lowest resistivity among the contact-metals used in MEMS industry and noble nature, can give us the reference line for testing other metals. With the results obtained after testing Au-contact under various conditions of applied load and cleaning, different contact-metals were compared with Au quantitatively for their contact resistance and stiction. The metal-pairs that can exhibit contact resistances closer to Au-contacts but lower adherence force until $\sim 10^8$ cycles can be termed as an electromechanically sound metal-contact pair. In our experimentation, because of the manual data acquisition method, contacts were tested until 10^6 or 10^7 cycles. The data acquired helps us understand the trends revealed by different metal-pairs under different conditions and compare them in order to find a better substitute for Au-contacts.

The experiments were conducted in two stages to understand the trends of electrical and mechanical curves during cycling tests.

- Stage One:- Four-wire resistance measurement in open ambient
- Stage Two:- *In-situ* and *ex-situ* cleaning of the metal-contacts under different plasmas and UV/Ozone followed by cycling

Stage One: - Stage one was very critical to understand the basic nature of A-B curves in different phases of contact-evolution for different metals. Figure 4.1 represents the most common A-B data-plot acquired after ~10cycles for an Au-Au contact loaded at 100 μ N from our system by using LABVIEW.



The most important steps while performing loading and unloading are represented by in orange color with numbers. At point 1, the piezo starts expanding in response to the waveform applied. From point 1 to point 2 piezo keeps on expanding due to a very small gap between the contacts. The bump does not come in contact with the pillar until point 2.

Figure 4.1 Sample Signal Acquired from AFM At this point, pillar mounted on piezo starts pushing the contact bump on the force sensor. The fixed-fixed beam structure thus bends in upward direction. This linear deflection is also associated with rotation, as explained in Chapter 2, making the laser beam deflect. Figure 4.1 shows the calibrated A-B signal. The beam further bends until it reaches point 3. Point 3 is the state of maximum piezo-expansion with respect to its driving voltage. In the mean while, the electric current flows from the contact when the contact is made at point 2 resulting in sudden resistance drop. Thus, from point 2 to point 3 completes one loading curve of one cycle. As we have applied a ramp signal for loading and unloading, piezo retraction starts from point 3. Loading force applied on the beam and hence the deflection decreases to move the laser spot downwards. It finally returns to its reference position. This is called as an unloading curve.

Ideally, the process of unloading should end here with point 4 lying at $0\mu\text{N}$ force. However, if metal surfaces, especially Au, are very clean then the film on the pillar gets stuck to the film that is coated on micro-bump due to the force of adhesion. The bonds developed during this process are very weak. However at micro-meter level the pull-off force is quite dominant over other forces. Therefore, the pillar starts pulling down the beam further and laser spot begins to deflect in negative direction. Contact between metallic counter-parts keeps the current flowing from circuit. Pillar keeps on going down while piezo is restoring and the beam bend further. This process continues until the bump experiences maximum pull from pillar. Just after this point *i.e.* point 4, weak bonds between the two suddenly break and the beam pops back to its original shape. Laser spot, accordingly, goes back to the reference position at point 5. Current flowing through the contact now stops as the two parts get isolated. From point 3 to 5, comprises of unloading phase of one cycle. Piezo further retracts until it comes back to its original shape *i.e.* point 6 in figure 4.1 when biased voltage gets zero. This entire process makes one complete cycle of switch-contact. If the contacts are not damaged due to yielding or material transfer then its separation after pull-off happens so quickly that, on the time scale, the A-B signal is acquired as a vertical line joining points 4 and 5. Hence, point 5 stands for maximum pull-off force recorded. Figure 4.1 is representing the same behavior with maximum pull-off force of $67.8\mu\text{N}$. Pull-off forces in the range of $100\ \mu\text{N}$ are normally considered as too high from switch-designing point of view.

For Au contacts, pull-off forces have been reported in the range of $20\ \mu\text{N}$ for the applied forces of around $50\ \mu\text{N}$ (30). Also a gradual increase in pull-off force up to $400\ \mu\text{N}$ has been reported by Gilbert (31) with the applied force in the range of 1mN when the Au switch-structure was cycled until 60,000 cycles under hot switching conditions. Efforts have also been made to report

the change in resistance for Au. Contact resistance reported by (8) is around $0.4\ \Omega$ with the applied force of $200\ \mu\text{N}$ while (14) $\sim 0.2\ \Omega$ to $0.3\ \Omega$ with the applied load of $150\ \mu\text{N}$. Kwon *et al* (11) were successful in measuring low resistance data however the load applied to achieve that was 50mN which is so high that is well beyond the practical consideration 100uN to 1mN . Dickrell *et al*(17) have made good attempt to measure the resistance and pull-off force simultaneously. Their test structure reports contact resistance of $930\ \text{m}\Omega$ at $150\ \mu\text{N}$ with the pull off force of $45\ \mu\text{N}$. All of the test set-ups mentioned here have used hot-switching conditions with $0.1\ \text{A}$ as sourced current. With a novel switch experiments performed at MIT, Kim (10) has recorded 0.1Ω resistance at $150\ \mu\text{N}$ until 10^{10} cycles. The purpose of the test-set-up built here in NEU is to test different material pairs under different forces after proper cleaning of the micro-contact. Following sections discuss the results of different tests performed on Au-contact. For convenience, the metal that is coated on the force sensor is stated first while the one on pillar side comes second separated by hyphen. For example Au-Ru means that gold is coated on force sensor while ruthenium is coated on pillar side.

Stage One: -

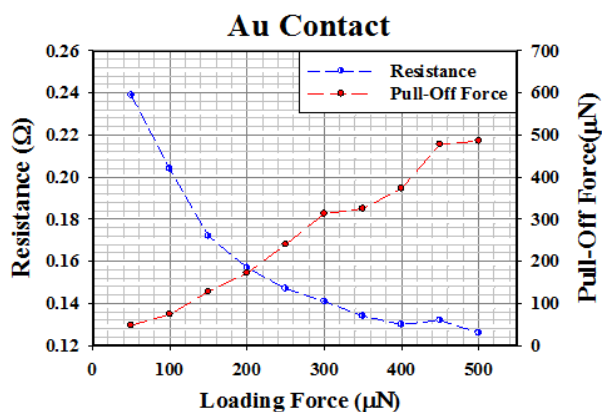


Figure 4.2 Au-Au Contact Resistance at Different Forces After ~ 10 cycles

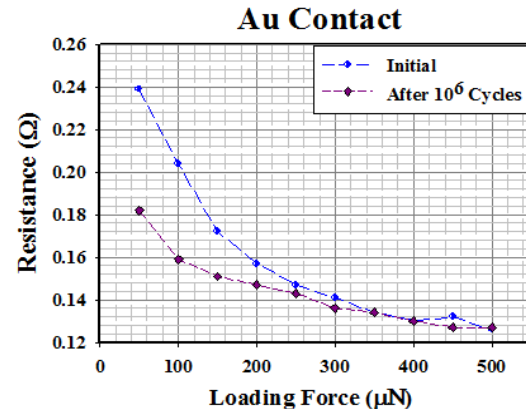


Figure 4.3 Au-Au Contact Resistance When Cycled at Particular Forces as Shown by the Bold Dots

This was the very first stage of the experimentation. In this stage Au-Au was tested under different loading forces in open ambient without doing plasma cleaning or UV/ Ozone cleaning. Freshly coated samples were used for conducting these tests without using N₂ ambient control. Since Au is resistant to most of the air-borne contaminants, strategy of using freshly coated samples was good enough to conduct the required measurements. The data shown in figure 4.2 is acquired by Dr. Chen before the contact underwent 10 cycles at particular force. As shown in figure 4.2 a typical Au contact exhibits contact resistance of around 0.2 Ω when loaded at 100 μN initially. Holm's theory states that the contact resistance decreases with the increase in contact area. This is clearly validated from the measurement-data shown in figure 4.2. Initially when 100 μN are applied on the contact, only a few asperities contact each other. The effective contact radius of ~0.2μm (27) causes the contact resistance of ~0.2 Ω. Repetitive switching (cycling) and application of higher force are the two modes of bringing more and more asperities into contact and increasing effective contact-radius. Both of these processes lessen the contact resistance in exponential manner. Figure 4.2 clearly shows the effect of application of higher force on contact resistance as well as pull-off force. Contact resistance decreases from ~0.2 Ω at 100 μN to ~0.13 Ω when loaded at 500 μN. At the same time, with increase in contact area, pull-off force increases in same proportion. Au contacts typically demonstrate the pull-off force in the range of 60 to 70μN with the application of 100 μN, at the beginning of cycling. Gold being very soft, the rate of increase of contact area is much higher for pure Au-Au contact than any other metal-pair. Hence, the adherence force increases very rapidly as the applied force increases. It is ~500μN for the Au-Au contact loaded at 500μN.

Figure 4.3 gives a wider picture of the decrease in resistance when contact is cycled at 100 μN . As shown in figure 4.3, the Au-Au contact resistance has shown decrease from $\sim 0.24 \Omega$ to $\sim 0.18 \Omega$ for the contact cycled at 50 μN and from $\sim 0.2 \Omega$ to $\sim 0.16 \Omega$ when the contact is cycled at 100 μN . It also illustrates that, as the loading force increases, the amount of decrease in contact resistance due to cycling decreases. In short cycling the contact until 10^6 cycles at 50 μN would exhibit significant decrease in contact resistance due to cycling. However if the same contact is cycled at 500 μN , the decrease in contact resistance would not be significant enough. This is due to the same reason as explained in previous section. The force of 500 μN is so high for an Au-contact that it brings most of the asperities into contact even at the early stages of contact-evolution. Cycling of such a contact until 10^6 does not make significant for the contact resistance. However contacts can fail to separate due to high stiction.

Stage Two: -

After understanding the general behavior of Au-Au contacts under different forces, the focus was given on performing plasma treatment on Au contacts. The purpose of this stage was to understand the effects of argon, oxygen, nitrogen and NF_3 plasma and UV/Ozone on Au and then to determine the appropriate treatment to clean the metal surfaces.

In-situ Plasma Cleaning Tests:-

The experiments were started in order to understand the *in-situ* plasma cleaning effects on Au-Au contact. The force sensor and pillar coated with Au were engaged by using AFM as explained in Chapter 3. Ar plasma at 0.3 lpm and 1750 mTorr was introduced while the contacts were switching at 100 μN at 1 Hz throughout the testing. Ar plasma was operative for 5 minutes. Contact-data was acquired at the interval of 1 min. After 5mins of Ar plasma, O_2 gas was

introduced into the chamber at 0.5 lpm to initiate the treatment under O₂ plasma. O₂ plasma was turned operated for 15 minutes and measurement was done at the interval of 1 min. After 15 min, O₂ gas was turned off and contacts were again treated under 5 minutes of Ar plasma for observing the changes in contact resistance and pull-off force. Thus *in-situ* cleaning had three stages: - 5minutes Ar plasma - 10minutes O₂ plasma - 5minutes Ar plasma.

Figure 4.4 shows the changes in contact resistance and pull-off force for an Au-Au contact during three stages of *in-situ* plasma treatment. Ar plasma did not show any significant effect on pull-off force and resistance almost remained unchanged for 5min. However, as soon as the O₂ was introduced sudden drop in pull-off force was observed while resistance increased gradually over the period of 15mins. This can be due to the presence of thin oxide film on Au surface (32).

Figure 4.5 reveals the rise in contact resistance from ~0.4Ω to ~1Ω after 15min of *in-situ* O₂

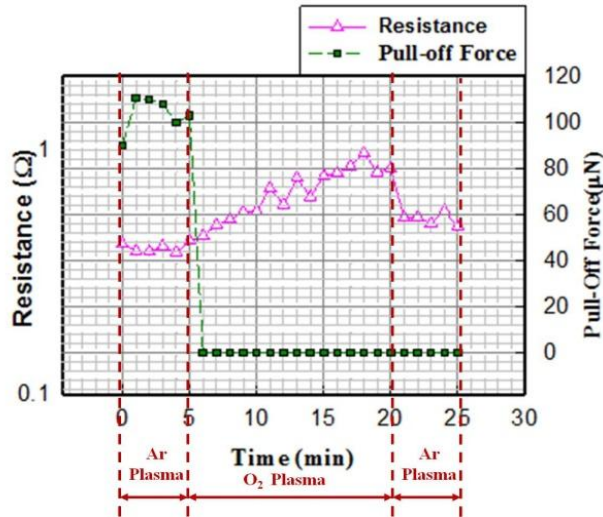


Figure 4.4 In-situ Plasma Cleaning Experiment on Au-Au Contact

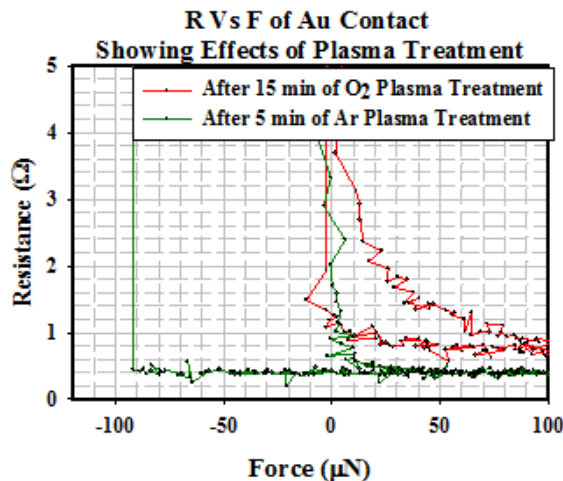


Figure 4.5 Resistance Vs Force Diagram Showing Effect of In-situ 15 min In-situ O₂ Plasma on Au-Au Contact

plasma cleaning. In these trials, the force sensor and bump were not exposed directly to the downstream plasma. This can reduce the effect of O₂ plasma treatment. Also, the plastic used inside AFM (as the part of tip-holder) and thermoplastic that is used to fix the piezo to the disc

might not be good. The active oxygen species present in O₂ plasma can react with the plastic to produce unwanted gasses and contaminants such as CO, CO₂ near the contact.

In-situ tests provided us with some understanding of the behavior of Au contact under Ar and O₂ plasma. In order to eliminate the possible sources of contamination in the *in-situ* tests, samples were cleaned by separately placing the plasma-chamber on a thick glass slab. This method was relatively simple and quick as compared to *in-situ* tests.

Ex-situ Plasma Cleaning: -

In these tests the chamber was placed separately on a glass slab. Samples were directly placed on the glass slab facing upwards such that the downstream plasma would directly bombard on the metallic layer. In this situation, only the samples remain inside. Hence all the probable factors such as thermoplastic from the holder, connecting wires, plastic from tip holder etc. that can cause the contamination are eliminated. Samples are directly exposed to the plasma stream instead of sideways like it was during *in-situ* plasma cleaning. All the experiments conducted under constant stream of N₂.

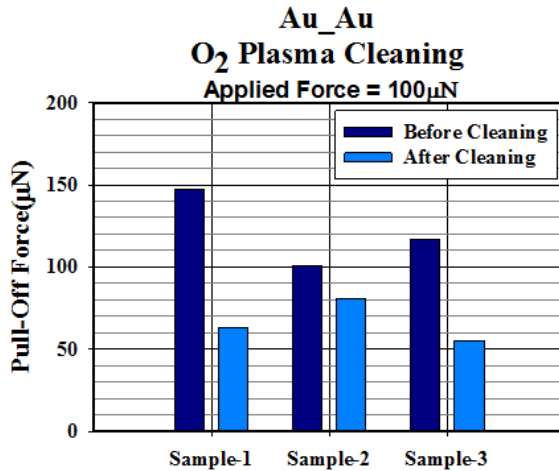


Figure 4.6 Au-Au Cleaning Effect of O₂ Plasma Cleaning on Pull-off Force

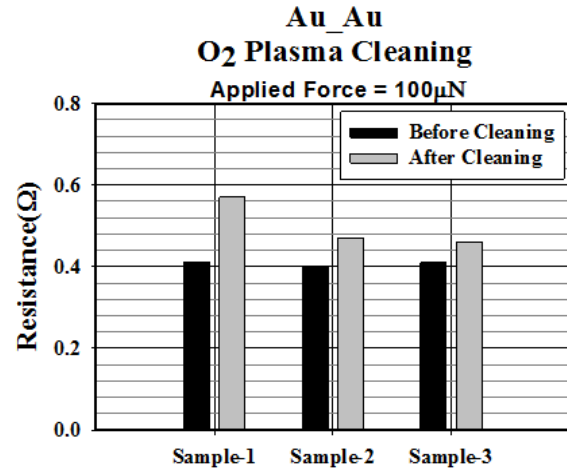


Figure 4.7 Au-Au Cleaning Effect of O₂ Plasma Cleaning on Contact Resistance

Since Ar plasma displayed its inefficiency during *in-situ* plasma cleaning, focus was given on observing effects of O₂ plasma on Au-contact. For initial trials, samples were treated under 3min of Ar plasma followed by 10 min of O₂ plasma. The cleaning was initiated with Ar plasma because that is requirement for switching on the plasma generator. The time interval of 3 min for Ar plasma was chosen arbitrarily. It gives the system enough time to stabilize. However it should be noted that this time *i.e.* 3 min is not very crucial for removing contamination when the cleaning are further going to be cleaned under 10 min of O₂ plasma treatment. Hence reduction of this time period does make any significant changes in contact resistances (after O₂ treatment). 3 min of Ar plasma treatment can be helpful only for removing the contaminants that are loosely bonded on the surface as explained in Chapter 1. After 3 min of Ar plasma, O₂ gas should be immediately turned on as explained in previous section. The pressures and gas flows were maintained at same levels as that were during *in-situ* plasma cleaning. It is important to note that the samples should be engaged as quickly as possible after treatment to avoid their exposure to moisture and other gasses in environment.

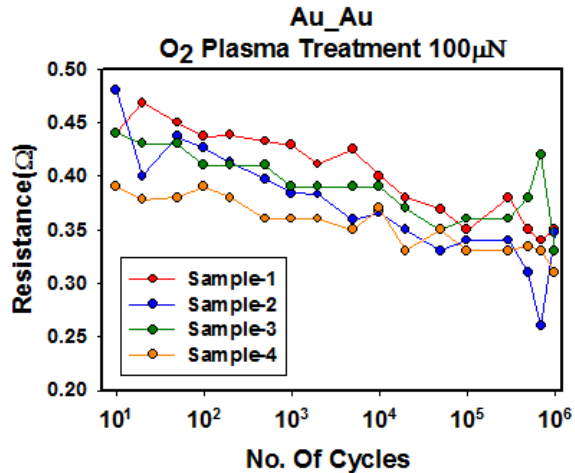


Figure 4.8 Au-Au Cycling Data Showing Resistance vs No. of Cycles

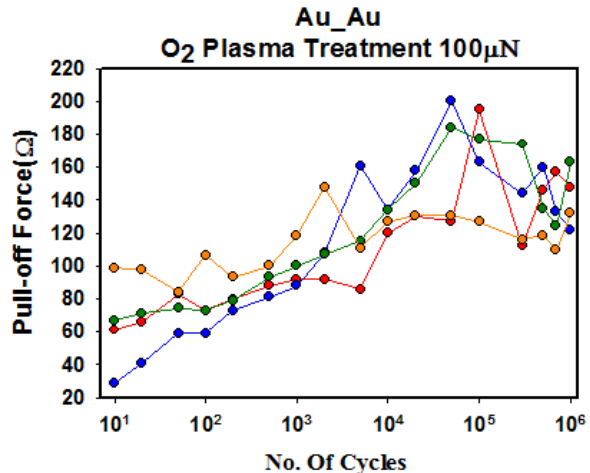


Figure 4.9 Au-Au Cycling Data Showing Pull-off Force vs No. of Cycles

Figure 4.6 represents the immediate effects of 3min Ar + 10 min O₂ plasma treatment for three samples Au-Au contact. Similar to *in-situ* cleaning results, Au-contacts have shown significant decrease in pull-off force and slight increase (by ~0.1Ω) in contact resistance as illustrated by Figure 4.7. Although Au is highly nonreactive metal and normally does not form its oxide on the surface. However, high energy particles present in oxygen plasma can form a very thin layer (few angstroms) of gold oxide (32), which can get destroyed with the repetitive loading or application of temperature above 50⁰ C. This is demonstrated by conducting cycling tests. Figure 4.8 demonstrates the trend of contact resistance during cycling of four such samples. These were treated under similar conditions of Ar and O₂ plasma and then cycled until 10⁶ cycles at 100 μN by following the frequency table given in chapter 2 (Table 2.1). The contact resistance has shown a consistent decrease during cycling. This shows that, the oxide film that can be formed during cycling gets ruptured easily. Since the cleaning mechanism of UV/ Ozone is similar to that of O₂ plasma, no experiments were performed for Au-contacts by using UV/Ozone.

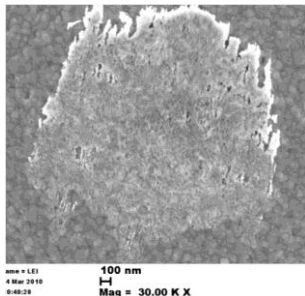


Figure 4.10 Sliding Occurring at Au-Au Contact Due to Misalignment

This can also be revealed by figure 4.9 which shows significant rise in pull-off force for Au-Au contact, especially after 10^3 cycles. At 10^5 pull-off forces are even in the range of $\sim 200\mu\text{N}$ which is extremely unfavorable for the contact-switches. It should be noted that alignment of the force sensor and bump exactly at 12° is very critical. Slight misalignment can produce sliding of the micro-contacts while switching as shown in SEM image (figure 4.10) taken by Dr. Chen.

This can lead to even higher pull-off forces due the damage of the surface film.

Types of Failures Observed in Au-Au Contact During Cycling Tests: -

High adherence force causes significant increase in pull-off force. Figure 4.11 shows one such example where an Au contact is cycled at $100\mu\text{N}$ until 10^6 cycles. During switching the pull-off forces were increased more than 3 times the applied load and made contact-separation difficult.

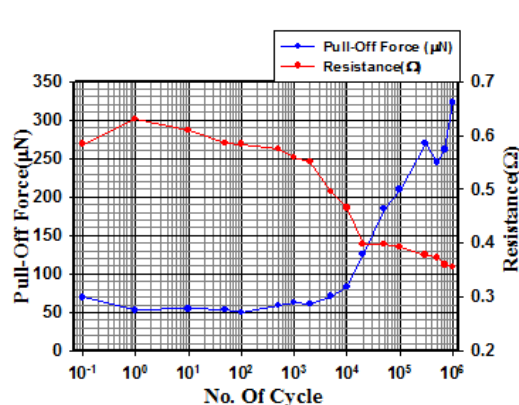


Figure 4.11 Au-Au Contact Showing High Pull-off Force During Cycling

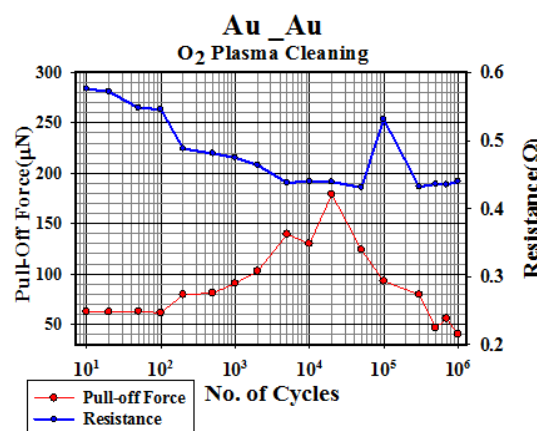


Figure 4.12 Au-Au Contact Ductile Separation

Figure 4.12 illustrates a contact-failure due to ductile separation. In this case also Au contacts were cycled at $100\mu\text{N}$ until 10^6 cycles. Pull-off force displayed abrupt variation during cycling

and causes increase in contact resistance due to necking. This was also revealed by the SEM images (not shown in this document).

4.2 Ru_Ru & Ir_Ir

Considering higher pull-off forces occurring in Au-Au contacts, the alternative is to search for a metal or combination of metals that can be promising from both the electrical and mechanical aspects. Refractory metals like Ru, Ir, Mb, Rh and Au-Ni alloys have recently caught attention and wide range of research has been going on to search for a better substitute for Au. The stages followed during experimentation were similar to those in Au contacts.

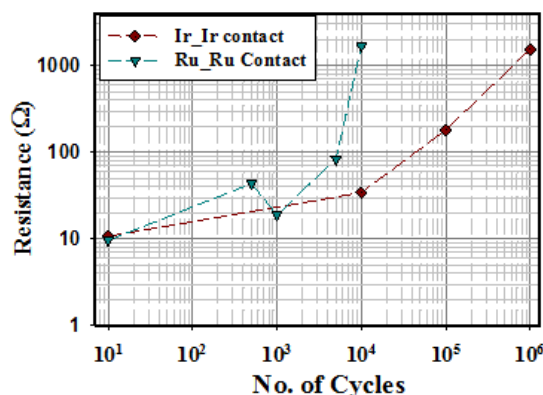


Figure 4.13 Ru & Ir Contact-Failures During Cycling

was 300nm on force sensor as well as on pillar. Considering that the metals are very hard as compared to Au, contacts were initially tested under higher forces ($500\mu\text{N}$) and then cycled. Neither plasma treatment nor nitrogen flow control was used during these tests. As represented by figure 4.13, the tendency of both the metals of getting contaminated was extremely high. The resistance started with very high value ($\sim 10 \Omega$) and just kept on increasing during cycling. No pull-off force was detected. Normally, contact resistance is very sensitive at lower forces ($\sim 100 \mu\text{N}$), especially for the contamination-prone metals like Ru, Ir. When the surfaces get

contaminated, applying higher forces ($>200 \mu\text{N}$) can break the contamination film that is formed on the surface. Since high-force testing itself displayed very high resistance values, low force testing at this stage was not done.

Stage Two: - The objective of this stage was to find out an appropriate cleaning method and determine a better candidate between Ru and Ir. After having chosen one, the next crucial task was to determine if this can replace Au in terms of resistance and under what operating force.

Similar strategy was implemented to compare effects of *in-situ* and *ex-situ* plasma cleaning on Ru-Ru and Ir-Ir contacts.

In-situ Plasma Cleaning :- Both the *in-situ* and *ex-situ* cleaning of Au-Au contacts had

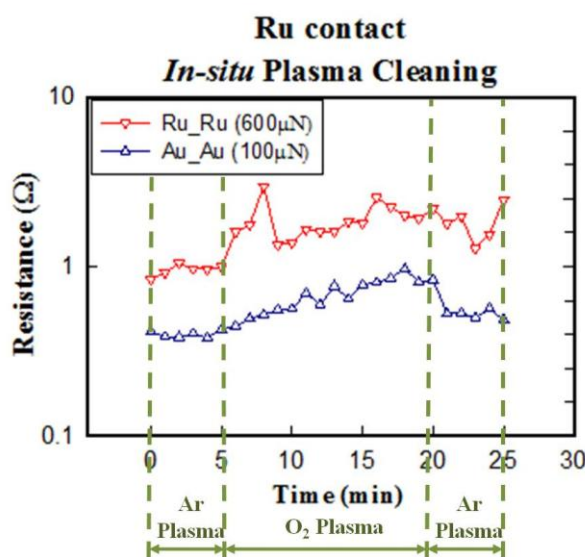


Figure 4.14 In-situ Plasma Cleaning of Ru-Ru Contact at 1 Hz

plasmas or UV/Ozone would be approximately same on both the metals. In order to understand the effectiveness of the plasma treatments, Ru was selected first. Fig 4.14 shows the result of *In-situ* plasma cleaning test:-In this test, force sensor and pillar were coated with a 300nm layer of pure Ru directly on Si substrate. Contact-bump was loaded at $600\mu\text{N}$ and cycled at 1 Hz while

displayed resistance-increase and drop in pull-off force immediately after Oxygen plasma treatment. However, Ar plasma did not show any significant changes. So, the efficiency of neither of the cleaning methods was confirmed during Au-testing. Ru_Ru and Ir_Ir had shown almost the same features when tested in open ambient (Figure 4.13).

So, the cleaning effect of either of the

the plasma treatment is going on. The trial was conducted in three stages 1) 5 min of Ar plasma cleaning 2) 15 min of O₂ plasma cleaning 3) 5 min of Ar plasma cleaning and the data was acquired at the intervals of 1min in similar manner as explained in previous section. 5min of Ar plasma did not show any change in contact resistance for Ru-contact. However it displayed immediate rise when O₂ plasma was introduced and remained higher ($>1\Omega$) until O₂ plasma was on. Contact resistance decreased slightly when O₂ plasma was turned off after 15 min. In short, the *in-situ* plasma treatment for Ru also failed to bring down the contact resistance and similar to Au slight increase in contact resistance was observed. The pull-off forces observed during the tests on Ru-Ru or Ir-Ir were extremely low ($\leq 5\mu\text{N}$). The inefficiency of *in-situ* plasma treatment can be because of the similar reasons given for *in-situ* cleaning of Au contacts.

Ex-situ Plasma Cleaning: - Ru samples were treated with both the plasmas (Ar and O₂) separately for different durations. These trials showed very clear decrease in contact resistance even for very dirty samples having initial resistance above 50 Ω before cleaning. All these tests were carried out by placing the vacuum chamber separately on a glass slab as explained in previous section. All the measurements were obtained under the constant stream of nitrogen.

Ar Plasma Treatment: -

Ar plasma treatment, in our set-up, can involve cleaning due by the heating due to the action of radicals and electrons that can only remove some of the loosely bonded contaminant particles and moisture. Ar plasma itself showed some remarkable cleaning result on Ru samples. Resistance can be further brought down by increasing the treatment duration. Figure 4.15 illustrates the effects of Ar plasma cleaning on Ru-contact. It also clear that time of treatment makes significant difference in reducing contamination. However Ar plasma, due to the lack to chemical reactions, has limitations on its efficiency. Even small traces of contaminating

molecules such as polymers, hydrocarbons etc. if remained on the contacting surfaces can be

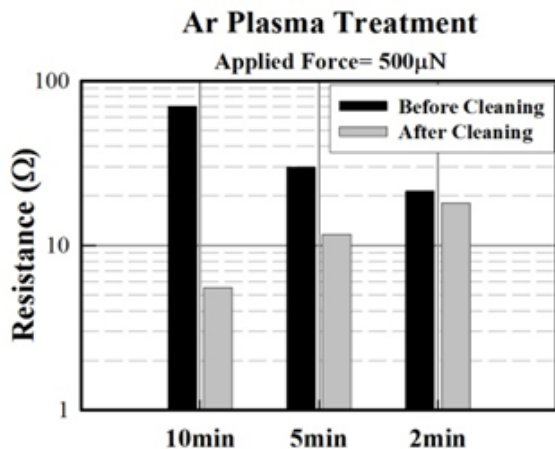


*Figure 4.15 Ex-situ Ar Plasma Cleaning Effect
on Ru-Ru Contact Resistance*

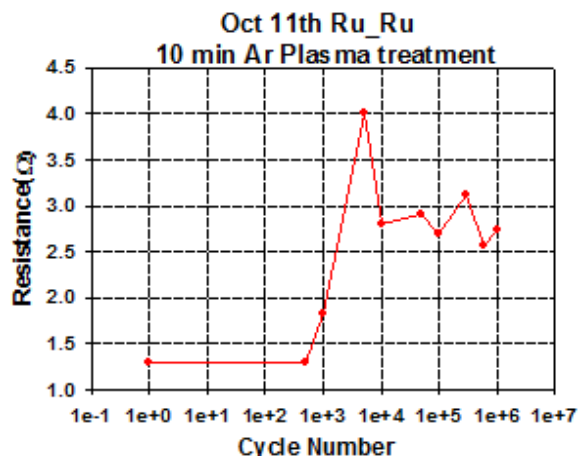


*Figure 4.16 Ru Contact Cycled at 500 μN
After Ar Plasma Treatment*

harmful. During switching with the current flowing across the contact, these molecules can build a contamination film which can again increase the resistance making the cleaning ineffective.

Figure 4.16 illustrates one such example of a cleaner Ru contact after 10 min of Ar plasma treatment but while cycling, the contact again got contaminated and resistance rose very quickly. In this case, even the application of 500 μ N was insufficient to break the contamination films those were formed on the surface during cycling.

O₂ Plasma Treatment:-

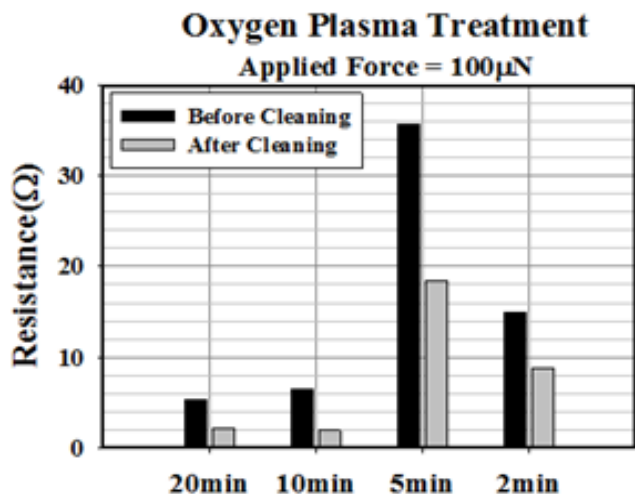


Figure 4.17 Ex-situ O₂ Plasma Cleaning Effect on Ru-Ru Contact Resistance

O₂ plasma, unlike Ar plasma, because of its dual cleaning action i.e. knock-out of the contaminants and oxidation reactions, becomes more effective as compared to Ar plasma. Figure 4.17 gives us an idea about the efficiency of O₂ plasma cleaning. It should be noted that all the contacts were first treated under 3min of Ar plasma before actuating O₂ plasma. Even two minutes of treatment was able

bring down the contamination-level significantly. It is important to note that the applied forces were 100μN in this case. O₂ plasma treatment followed for 10 minutes and 20 minutes showed remarkable difference in the cleaning-efficiency as compared to Ar plasma-cleaning. A few trial were also taken with 20min of O₂ plasma but it did not prove to be significantly effective than 10 minutes shown in figure 4.17. Figure 4.18 shows an example of substantial decrease in contact resistance after *ex-situ* cleaning for 3 min of Ar + 10 minutes of O₂ plasma treatment on Ru contact loaded at 100 μN. Normally when a contact is loaded, the contact resistance decreases with the increase in load due to the increase in contact area. So, when the contact is unloaded from the same force, the contact resistance should follow the same path as it was during loading. However in our set-up we have typically observed a slight decrease in contact resistance during unloading phase especially for the contacts before cleaning as shown in figure 4.18. The exact reasons behind this phenomenon are unknown. However it is speculated that the minor errors during micro-fabrication can make the force sensor (and hence the contact-bump) asymmetric

about the center. This can lead to slight rolling of the micro-contacts during unloading phase. The effects can be more prominent if a thin contaminant-film is present on the surface leading to decrease in contact resistance while unloading.

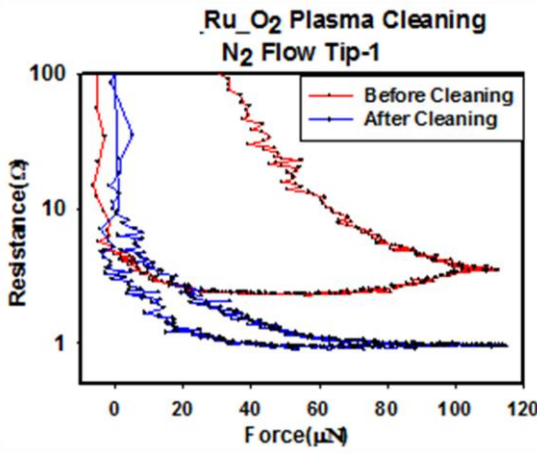
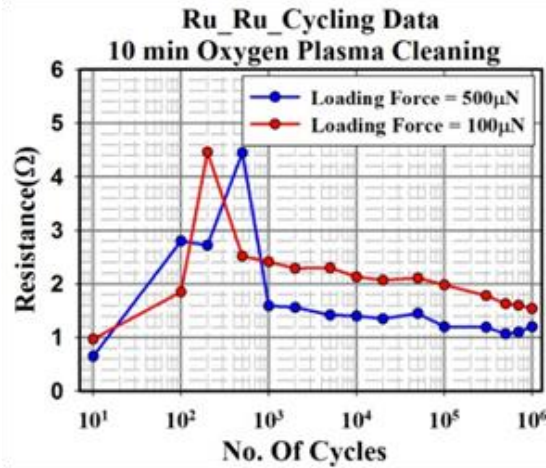


Figure 4.18 Cleaning Effect of O₂ Plasma on Ru-Ru at 100 μ N



4.19 Cycling Data of Ru-contact After O₂ Plasma Treatment

Resistances were measured consistently $\sim 1\Omega$ when contacts were loaded at 100 μ N and $\sim 0.8\ \Omega$ under the loading of 500 μ N after cleaning (figure 4.19). As a common trend of a Ru-Ru contact during cycling (after 10min O₂ cleaning), a sharp rise in resistance until 10³ cycles was observed followed by a sudden drop and then steady descent in resistance as the typical trend for Ru contacts. Fig 4.19 illustrates the same phenomena for two tips loaded at 100 μ N and 500 μ N respectively. We never observed any pull-off force for Ru-Ru and Ir-Ir contacts.

UV/Ozone involves similar oxidation reactions. However it was not as effective as O₂ plasma as illustrated by figure 4.20 that gives quick review of three methods. For making UV/Ozone cleaning more effective, distance of the samples from source, pressure conditions and Oxygen flow should be maintained very accurately (22). Figure 4.20 indicates the comparison of three

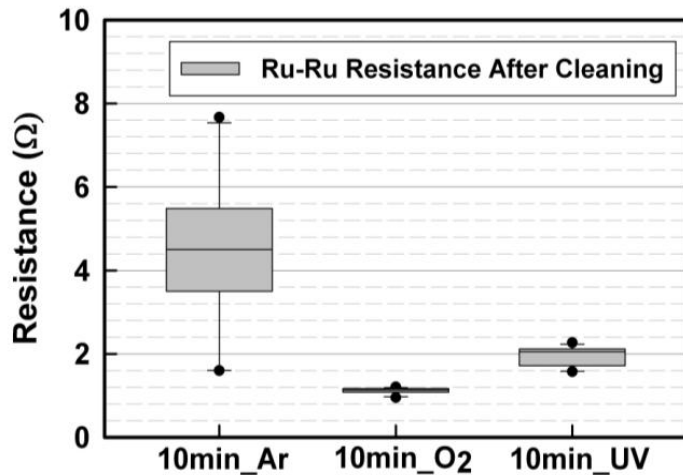


Figure 4.20 Comparison of Three Cleaning Methods

Finally it was concluded that, for our system, the treatment of 3 minutes of Ar plasma followed by 10 min of O₂ plasma was sufficient enough to clean the surfaces after proper handling of samples during fabrication. It is worth to note that, if the resistance vs. force curve after cleaning does not look nice and flat as shown in figure 4.18, one should follow one more cycle of 3min of Ar plasma and 10 min of oxygen plasma treatment.

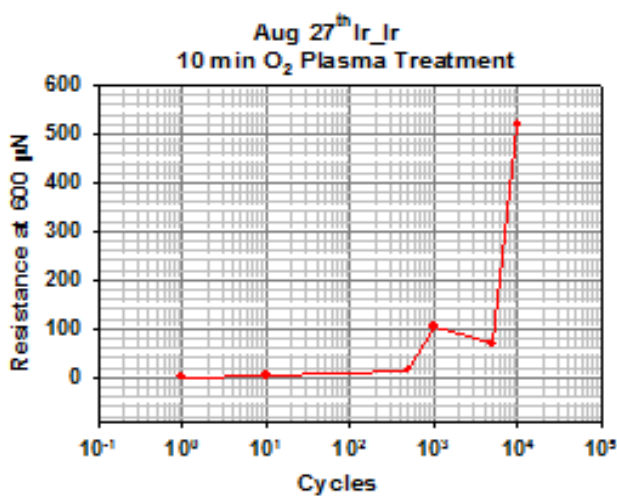


Figure 4.21 Cycling Data of Ir Contact After O₂ Plasma Treatment

cleaning methods carried for 10 min when Ru-Ru contacts are tested at 100μN. Close distribution of contact resistances ~1Ω after 10 min of O₂ plasma treatment clearly displays its over UV/Ozone and Ar plasma cleaning.

After the successful trials of O₂ plasma on Ru-contacts, the same strategy and methods were applied on Ir-contacts. O₂ plasma was able to bring down the Ir contact resistance below 1Ω. However it did not sustain for many number of cycles. Ir-Ir contacts have displayed rapid contamination- failure. Figure 4.21 shows one such example of Ir contact that was treated for 3 min of Ar + 10 min of O₂ plasma treatment.

Even, the application of 600 μ N failed to provide stable contact resistance and displayed quick rise after only 10^4 cycles when tested under N₂ ambient control.

Our second stage was finished here with the conclusion that 3min of Ar + 10 min O₂ plasma treatment was better than Ar plasma and UV/Ozone cleaning. It also confirmed that Ru-Ru contact are reliable than Ir-Ir contacts even at low forces (100 μ N). Although Ru-Ru did not display any stiction as that in Au-Au, resistances recorded were much higher than Au. This can be a limiting factor in its usage as a contact metal in MEMS switches.

4.3 Au_Ru & Au_Ir

As explained in previous section, using only Ru or Ir on both sides for contact did not provide any promising results from reliability point of view. Ru showed some features that proved it superior than Ir to some extent. However if one is looking for a better substitute for Au for MEMS applications then lower resistances (~0.2 Ω to 0.3 Ω) at lower forces (~100 μ N to 150 μ N) should be achieved. The metal-pair should exhibit lesser adherence. While using a combination of two metals, it is critical to decide their locations. Two factors were considered while taking the decision. Ru, when deposited on beams develops residual stress (33). This stress causes the beam to buckle in upward direction. Controlling pressure during Ru-deposition for fabricating stress-free unbuckled beam was found to be very tough. Similar was the case for Ir deposition but the buckling was in opposite direction due to the compressive stresses. This phenomenon puts obstructions while doing the engagement. There is always a big possibility of the edges of pillar contacting the bump from sideways. Au films, on the other hand, do not put any stress on the structures. Hence the beams always remain perfectly flat after deposition. Controlling the deposition conditions for Au is easier than that for Ir or Ru.

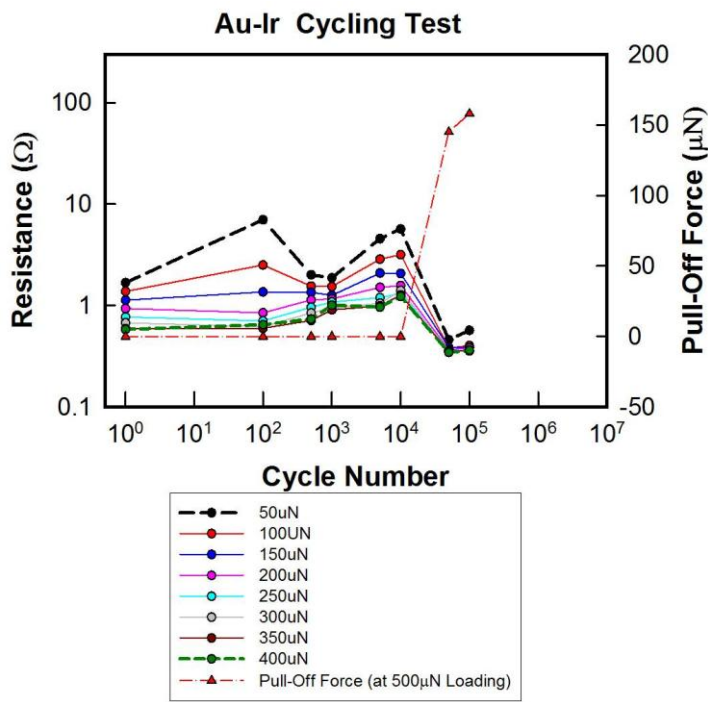


Figure 4.22 Cycling Data of Au-Ir

after few switching cycles. In this case controlling the switching force becomes an important issue. Application of larger force ($\sim 500 \mu\text{N}$) can damage the tip due to yielding.

In order to avoid both the possible factors that could affect smooth engagement during testing and life-time of the contact-pair, Au is selected as the material on the force sensor with Ru or Ir on the pillar.

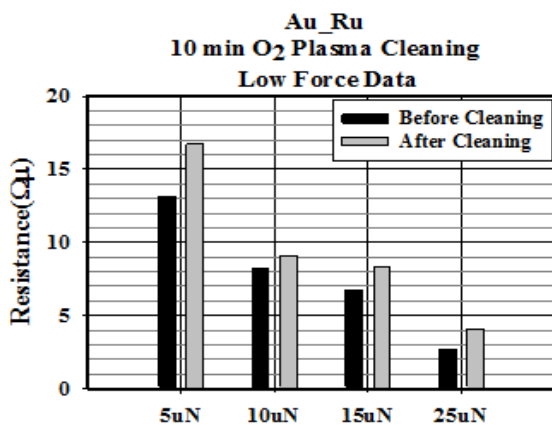


Figure 4.23 Au-Ru Low-Force Contact Resistance Measurement

The second reason behind selecting Au for the force sensor was its soft nature. As the contact-area increases due to flattening and regrouping of asperities during cycling, using Au-bump on Ru-pillar is just like a soft ball is getting pressed against a hard surface like floor. So, theoretically it is expected that the contact resistance will drop reasonably

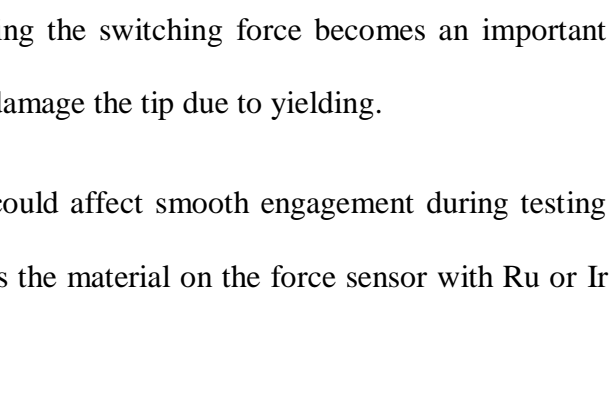


Figure 4.24 Au-Ru Cycled at 100μN

In this approach of using different metal pairs on both sides, O₂ plasma cleaning was used in all the experiments because it was clearly proved to be efficient over argon plasma and UV/Ozone cleaning. So, the sample were first tested for resistance values and then cleaned under argon plasma for 3 minutes followed by oxygen plasma for 10 minutes.

Figure 4.22, plotted by Dr. Chen, corresponds to an Au-Ir contact loaded at 400 μ N and then cycled after cleaning. Data is collected also at different forces. Ir shows its inability to reach to lower value of contact resistance (at 100 μ N) than Au-Ru, in this case as well. Although it shows

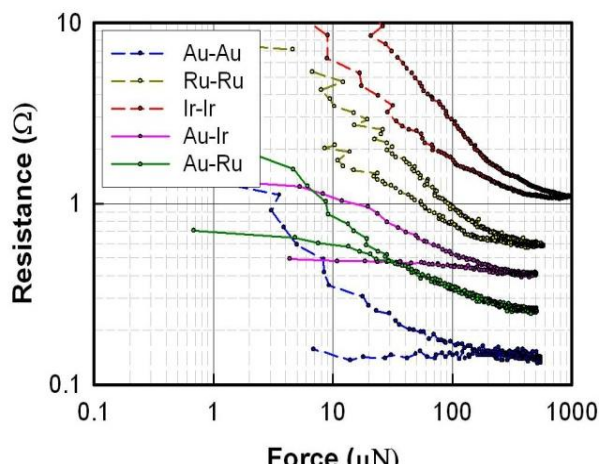


Figure 4.25 Comparison of All Materials After O₂ Plasma Cleaning

sub-ohm resistances when loaded at 400 μ N, the contact fails only after 10^4 cycles due to larger pull-off force. However, as we can see in Figure 4.23 that, Au-Ru contact were able to deliver very low resistances even at very low forces (25 μ N). The combination of Au on Ru has proved to be very effective when applied forces were in the range of 100 μ N. They have shown consistent

drop in contact resistance during cycling while the pull-off force did not vary much and remained in range of 60 to 70 μ N (Figure 4.24). The highest pull-force recorded being ~97 μ N after 10^4 cycles in Figure 4.24. This testing, again revealed that Au-Ru is reliable considering low electrical resistance at low forces (~100 μ N) and lower pull-off forces as compared to Au-Ir. Among all the metal-contact pairs tested so far Au-Ru has consistently given us low resistance measurement. Au-Ru contact- resistance was observed to be slightly higher (by ~0.2 Ω) than Au contacts but their lower stiction as compared to Au-Au gives it added advantage. Figure 4.25 provides a quick review of all the metal pairs, in terms of contact resistance when loaded at

500 μ N after performing 3min Ar + 10min O₂ of plasma cleaning. Figure 4.25 clearly reveals the importance of using Au as one of the contact metals with pure metals, Ru-Ru and Ir-Ir showing comparatively higher resistance.

Ke *et al* (9) have also used Au with Ru. However they have pursued with a novel approach of using a layered stack of 50nm Ru over

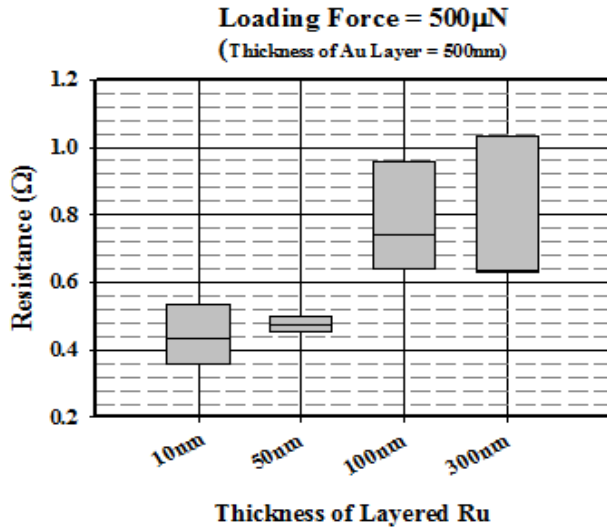


Figure 4.26 Distribution of Contact Resistance Data of Layered Au/Ru

500nm of Au. The resistance reported is ~0.8Ω with the application of 400 μ N.

Taking inspiration from this idea we further continued our experiments to find the best possible combination for the layered stack of Ru so as to achieve lower resistances and pull-off forces. During

these trials we used four different types of Ru layers *i.e.* 10nm, 50nm, 100nm and 300nm coated over 300nm of Au. However, pillars are already electroplated with 500nm of Au to minimize the sheet resistance effect arising from pillar-walls. So, on pillar the total thickness of electroplated plus sputter coated Au becomes 800nm.

Au being the softer metal on both the sides deforms more than pure Ru-contact during cycling because of the thinner Ru layer. So, the contact radii of 10nm and 50nm Ru thicknesses are much higher than that of 100nm and 300nm layered Ru at corresponding forces. This can be seen from simulation results given in Chapter 3 (Figure 3.6). Considering simulation results for layered Ru from Chapter 3, it was expected that 10nm and 50nm stack of Ru would demonstrate lower resistance than 100nm and 300nm. Figure 4.26 represents the distribution of contact resistance data acquired at 500 μ N after 10min of O₂ plasma cleaning for 6 samples. Although it shows some uniformity in the 50nm layered Ru case, in other three cases it is widely distributed.

Figure 4.27 compares layered Ru with Au-Au, Ru-Ru and Au-Ru contacts after 10min of O₂

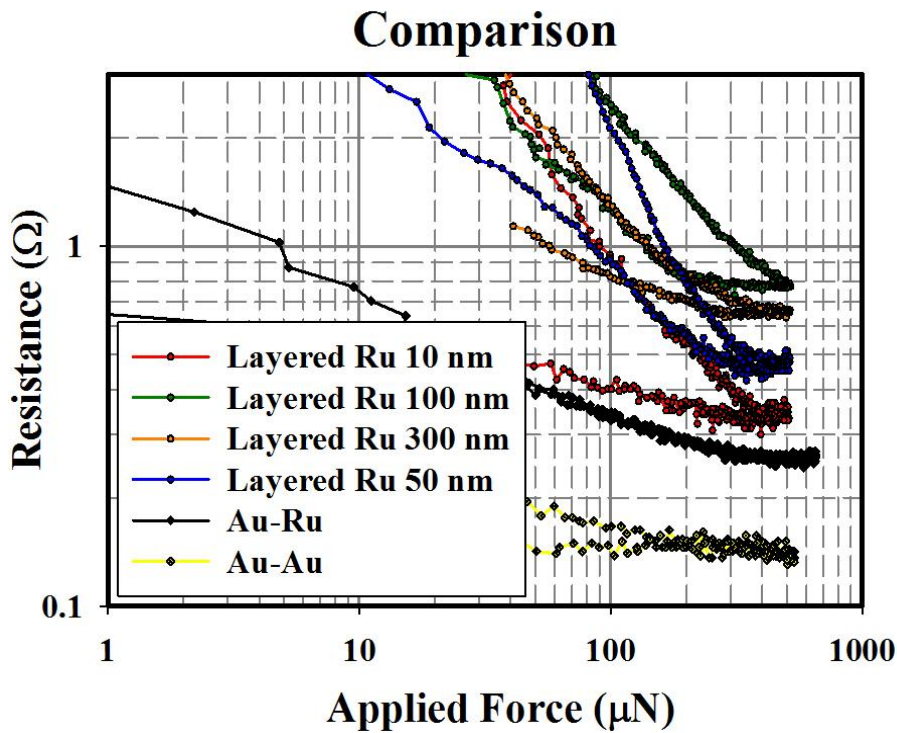


Figure 4.27 Comparison of Au-Ru With Layered Au/Ru

plasma cleaning when loaded at 500 μ N and indicates that Au-Ru contact resistance goes quite nearer to pure Au-Au. Pull-off forces were never observed in all of the four types of metal-stacks. Although this novel metallization stack provides us some promises considering its low resistances and no stiction, more experiments are required to be conducted for determining appropriate thickness of Ru over Au to operate under different conditions of load.

4.4 Vanadium Oxide

Lin *et al* (34) have been doing the research on finding a reliable contact-metal pair that will have very low resistance and pull-off force at lower loading force. In this approach an alloy of vanadium oxide (V_2O_5) and Au film is used as contact-metal. Testing with this alloy has revealed significant improvement in the grain structure and decrease in pull-off force even at elevated temperatures (~400 $^{\circ}$ C). The same material was tested with our set-up. 3min of Ar plasma and 10 min oxygen plasma cleaning showed slight drop in resistance and rise in pull-off force after treatment (Figure 4.30). Four samples were tested in this manner and all of them demonstrated the same trend that confirmed the efficiency of cleaning. One sample that was not treated with plasma failed during cycling due to contamination as illustrated by Figure 4.28. The contamination resulted in reduction in adherence and increase in resistance because of the formation of film in between contacting parts. All of the cleaned samples showed a very consistent resistance measurement (~1 Ω) until 10^7 cycles. Adherence was regularly recorded below 100 μ N. Small amount of sliding was observed during cycling tests due to slight difference in angle in two mating parts. This sliding may have resulted in somewhat higher pull-off forces than that of claim by (34). In short, the layer of vanadium oxide on Au did show

remarkable improvement in reducing stiction problem but higher resistances at lower forces can put some limitation on its usage a contact-metal pair in MEMS switches

Only a few trials were conducted to test this material because of the limited number of samples available. More tests under different loading forces are required to be done. Au/Vanadium oxide on Au can also be an interesting pair to investigate with our system.

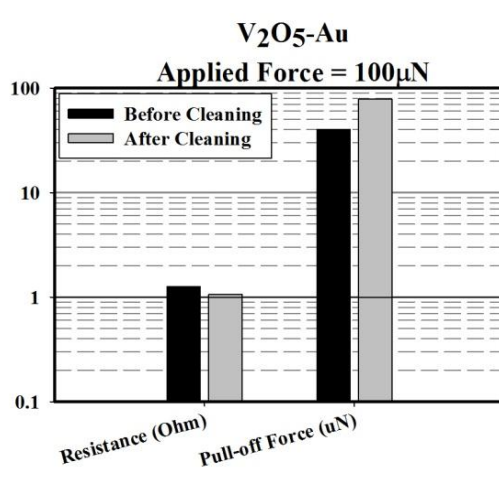


Figure 4.28 Au/ V₂O₅ Showing Effect of O₂ plasma Cleaning

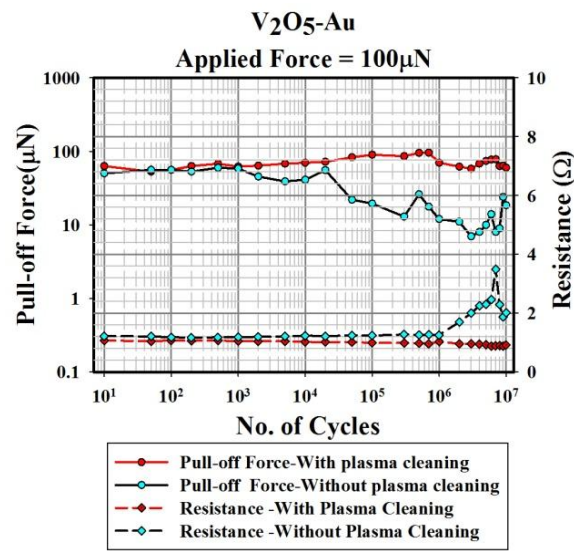


Figure 4.29 Au/ V₂O₅ Cycling Data

4.5 Au-Ni Alloys

Au_Ni alloys, recently, have caught attention in the MEMS field. These are usually two phased alloys which are expected to provide lower stiction as compared to Au. Contact resistance

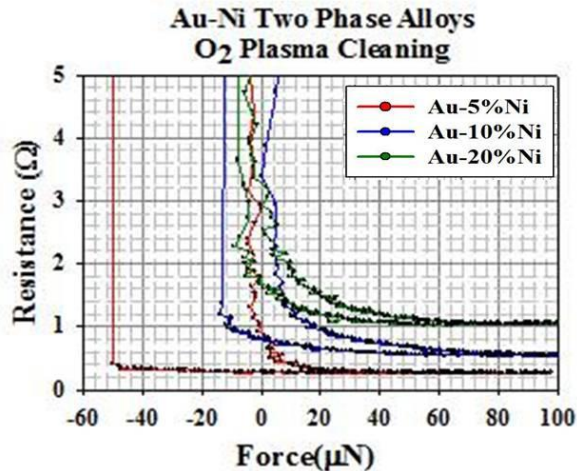


Figure 4.30 Au-Ni Alloys' Contact Resistance Comparison After O₂ Plasma Cleaning

however increases depending on the amount of Ni(14). Figure 4.30 shows the increase in initial contact- resistance and decrease in pull-off force as in % Ni in Au increases. Yang *et. al.* (14) have reported improved life time and reduced wear rates by using Au-Ni (20 at %) as contact material as compared to Au-Au. According to data presented by (8)Au-Ni (5 at %) at 200 μN

have shown contact resistances in the range of ~1.1Ω and almost no pull-off force. Schimkat from (1) have measured very low contact resistances for Au-Au-Ni₅ when loaded in the range of

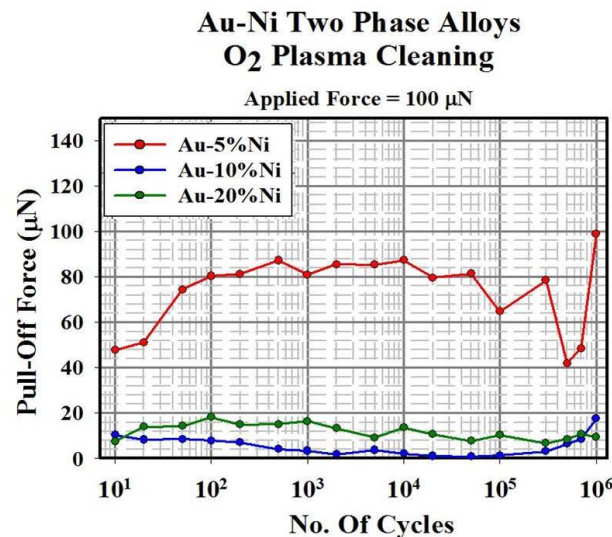


Figure 4.31 Au-Ni Alloys' Cycling Data Resistance vs No. of Cycles

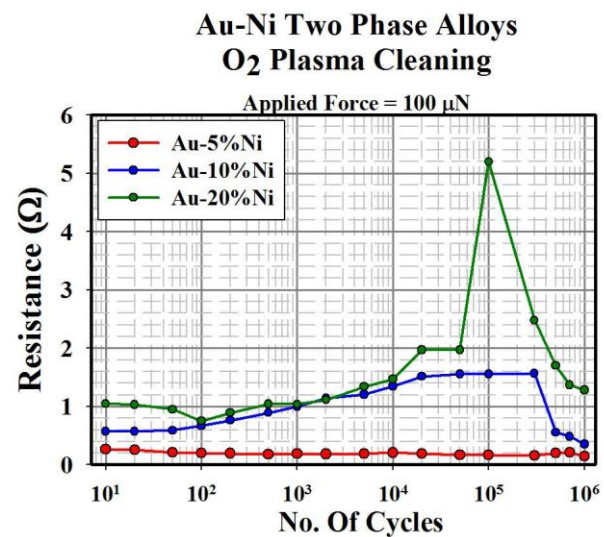


Figure 4.32 Au-Ni Alloys' Cycling Data Pull-off Force vs No. of Cycles

100 to 500 μ N. Tests done here with our set-up compare Au-Ni alloys having three different compositions namely Au-Ni (5 at %), Au-Ni (10 at %), Au-Ni (20 at %). All the samples were treated with 3 min of Ar plasma followed by 10min or O₂ plasma before cycling. Figure 4.31 reports the trend of pull-off force during cycling. As the amount of Ni (by %) increases pull-off force decreases but resistance increases (figure 4.32). Thus, Au-5% Ni gives least resistance ($\sim 0.2 \Omega$) among these three types but it is also associated with the pull-off forces in the range of $\sim 80 \mu$ N.

Chapter 5- Conclusions

MEMS technology has shown very promising features as compared to the solid state devices such as GaAs FET, and P-I-N diodes as far as the isolation, resistance, power consumption and losses are concerned (2). However they have not been able to completely substitute the solid state devices because of the reliability issues. These issues are mainly categorized into ‘failure to open’ or ‘failure to close’. Different metals exhibit different modes of contact failure depending on the operating conditions.

In order to study aforementioned failure mechanisms during contact evolution a test facility is built as a part of this thesis work. This facility is equipped with the simultaneous measurement of force applied at the micro-contacts and four-wire contact resistances across them by incorporating specially designed micro-contact test structures into JEOL SPM. These structures were coated with a variety of different metals and operated by piezoelectric actuation to imitate the functioning of a MEMS contact switch. The test system is also provided with a plasma generator for performing gas-plasma treatments by using three gasses *i.e.* Ar, O₂, and NF₃, and a deuterium lamp for creating UV/Ozone to remove the contaminants from the surface. Nitrogen flow control is used to control clean ambient around the contacts while performing switching.

Cleaning test performed on several metal-pairs revealed that O₂ plasma is more effective than Ar plasma and UV/Ozone. NF₃ plasma was found to be very strong. It peeled-off the metal film from the samples during cleaning. Hence, the experiments with NF₃ plasma were not continued further. The trials on cleaning methods also concluded that 3min of Ar followed by 10min of O₂ plasma was sufficient for removing the contamination that can occur with our samples when they are handled properly during fabrication processes. Although Au contacts provided us with very

low contact resistances ($\sim 0.15 \Omega$), they have shown a consistent increase in pull-off force and decrease in contact resistance due to the increase in contact area during cycling tests. Both the Ru and Ir contacts showed drop in contact resistance during cycling. The measured pull-off forces were extremely low ($< 5 \mu\text{N}$) for either of these materials. Ru was found to be better than Ir considering its contact resistance and reliability. Tests were conducted on different metal-contact pairs to achieve low contact resistances similar to Au with low pull-off forces. The metal pairs included Au-Ru, Au-Ir, layered Ru, V_2O_5 -Au alloy, Au-Ni alloys with 5%, 10% and 20% of Ni in Au respectively. Among all the metal-pairs listed before, Au-Ru pair can be an electromechanically reliable pair having maximum pull-off forces of $\sim 80 \mu\text{N}$ and contact resistances in range of $\sim 0.2 \Omega$ to 0.3Ω when cycled at $100\mu\text{N}$.

Simulations performed by using Ansys 11.0 illustrated that the effect of spreading resistance in the thin films increases the overall contact resistance if the contact-radii are not small as compared to the film thickness. Simulations conducted on real geometries having 300nm film-thickness of Au and Ru respectively for estimating the contact resistances when they are loaded at $100 \mu\text{N}$ and $500 \mu\text{N}$ revealed the close agreement of measured contact resistances with those predicted by Ansys. Also, the model for estimating the resistances of layered Ru as given by Ke *et al* (9) very closely resembles with the Ansys-simulated data. This model indicated the decrease in contact resistance of the layered Ru contact with the decrease in Ru film thickness over Au at corresponding forces.

With this work it can be concluded that, although the Au-Au contact pair exhibits very low contact resistances, it is not suitable for RF MEMS applications due to the high pull-off forces. Ru-Ru can provide us with very low pull-off forces and high reliability if the contacts are cleaned properly and tested under a laminar stream of nitrogen. The experiments conducted on

layered Ru have shown that Ru-Ru contact resistances can be reduced by coating a thin Ru film on Au. Layered Ru having film thickness of 50 nm of Ru on 300 nm of Au has shown some promising results for reducing the contact resistances and pull-off forces. More experiments are required to be done in order to consolidate superiority of layered Ru with 50 nm of Ru on Au over 10 nm, 100 nm, and 300 nm of Ru on Au. For reducing the pull-off forces occurring in Au-Au contacts, Au can be alloyed with Ni. Pull-off forces were decreased while contact resistances were increased with the increase in Ni by % in Au. Although Au with 5% Ni displayed better performance than Au with 10% Ni and Au with 20%, it is recommended that more testing should be done to confirm it. Au-Ru contact pair has consistently shown lower contact resistances and better reliability than most of the metal contact pairs (Au-Au, Ru-Ru, Ir-Ir, Au-Ir, Au-V₂O₅, and Au-Ni alloys) tested during this work.

Chapter 6- Future Work

The test set-up assembled during this work provided us with the ability to conduct variety of tests on different metal-contact pairs. The plasma cleaning experiments and N₂ proved very efficient to reduce contamination failure. However, manual data-acquisition method puts limitations on the cycling test. It requires ~ 40 minutes to finish 10⁶ cycles and more than 3 hours for 10⁷ cycles. However in reality a contact is expected to survive 10⁸ switching cycles to be termed as a reliable contact-pair. The phenomenon of piezo-drift that requires manual adjustment of D.C. bias voltage can be overcome by improving the LabVIEW program. With the help of a feedback control to adjust the D.C. bias or amplitude of the waveform from signal generator would serve the purpose.

All the testing was performed by performing hot-switching at 0.2V across the contacts. Although such a low voltage does not cause any trouble to the contacts (4), in the next step, it is required to understand the contact-evolution by performing cold switching cycling experiments.

Effects of temperature on micro-contacts are another important dimension in micro-contact studies. Applications such as cell phones where temperatures rise considerably higher than ambient temperature, these studies will prove very effective. A facility such as inline heater or blower with temperature adjustment, that can focus the hot N₂ stream directly on contact structures would give us understand the behavior of different metals in better manner.

Au-Ru results have indicated that this metal-pair has the potential to be used as a substitute for Au. Layered Au/Ru have also shown similar trends. More experiments are required to be done on these pairs for understanding the range of contact resistances for particular thickness of Ru.

Also it will be a good idea to try Ru layers with thicknesses 20nm, 30nm, 40nm etc. for understanding effect of film thickness on contact resistance.

Appendix A

Calculation for Nitrogen Flow Control

Since the concept of using nitrogen ambient to isolate the contact-area from atmospheric contaminants is taken from the research performed by Lei (5). Similar assumptions are used for estimating the concentration levels near contact. A laminar stream of nitrogen is introduced to the contact area by using a small tube. Following is the data that used for calculation purpose. Organic molecular concentration in the air, C_0 , was compared with the concentration near contact C_A . As the contaminants slowly diffuse into the laminar stream of N_2 , its concentration decreases parabolically (*figure A1*)(5). Diffusion coefficient, D_{ab} for Benzene is assumed as $0.102 \text{ cm}^2/\text{sec}^{-1}$ and nitrogen flow thickness of ~0.5 times the pipe diameter considered.

- Diameter of the pipe carrying $N_2 = \frac{1}{4}''$
- Cross sectional area of the tube that focuses N_2 on the sample = $3/16 \times 3/32$
- Diffusion coefficient value of benzene in Nitrogen = $D_{ab} = 0.102 \text{ cm}^2/\text{sec}$
- Flow of $N_2 = 0.9 \text{ lpm}$
- Velocity of N_2 flow = $V_{flow} = 1.3 \text{ m/sec}$
- Distance of the sample from tube = ~2mm
- Nitrogen flow thickness is considered as half of the tube thickness = $T = 1.2\text{mm}$

$$\frac{c_A}{c_0} = erfc \left[\frac{T}{\sqrt{\left(4.D_{ab} \cdot \frac{L_{path}}{V_{flow}} \right)}} \right]$$

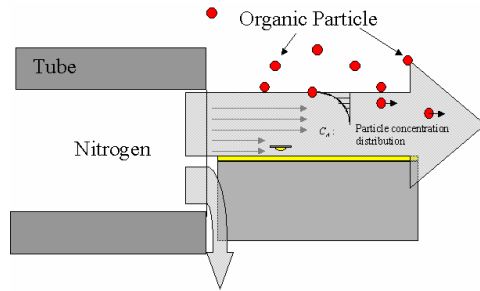


Figure A1 Concentration Profile

Based on the above calculations, the concentration level of organic contaminants was ten orders of magnitude lower than that in air. It is important to note that the samples remain on the corresponding holders at the angle of 12^0 to the flow. They are always switching while conducting the tests which can make the laminar flow unsteady. Hence, the calculations given above only give some estimation of the efficiency of N_2 flow. For the simplicity in calculation for determining the turbulent flow regime, Reynold's number (R_e) is assumed to be 580 for steady jet flow (42). Pipe radius assumed to be equal to 2 mm and kinematic viscosity for nitrogen can be taken as $1.52 * 10^{-5}$ m²/s (43). Q can be calculated from Re as,

$Q = \frac{R_e L}{v A}$ where Q is the flow rate, L is the characteristic length of pipe i.e. pipe diameter, v is kinematic viscosity of nitrogen and A is cross sectional area of pipe. Based on this calculation the limiting flow can be estimated as 1.62 lpm before it gets converted into turbulent regime.

Appendix B

Calculations for Designing Roughing Hose Diameter

The specified chamber-pressure for turning on the plasma-generator for Ar is 1 to 4 torr and the flow of the gas required is 1 to 4slpm. Since the system is used for different gasses with Ar continuously flowing through the plasma-generator, for the design purpose, it is assumed that the chamber will be maintained at 2 torr with the total flow of the gas equal to 3slpm. The working as is considered as air.

i.e. $Q = 3 \text{ slpm} = 0.05 \text{ lps}$

Assuming viscous flow,

Conductance, C for the hose is given as (35),

$$C_{\text{air},20}^0 = 135 \cdot \frac{d^4 \cdot P'}{l} \text{ L.s}^{-1}$$

For our system, length of the pipe = 120 inch

$$P' = \frac{P_1 + P_2}{2}$$

Where P_1 = Pressure maintained inside the chamber = 2 torr

P_2 = Pressure downstream = 100mtorr (assumption)

Hence, $P' = 1.05 \text{ torr}$

$$C_{\text{air},20}^0 = 135 \cdot \frac{d^4 \cdot 1.05}{120} \quad \dots \dots \dots \quad (1)$$

The resistance offered by the length pipe is defined by (36),

$$R = \frac{P_1 - P_2}{Q} = \frac{2 - 0.1}{0.05}$$

$$R = 38 \text{ torr.s/l} \quad \dots \quad (2)$$

$$C_{\text{air},20}^0 = \frac{1}{38}$$

Comparing equations (1) and (2)

$$d = 0.4 \text{ inch}$$

However, the smallest inner diameter of the commercially available roughing hose was 0.74" with the outer diameter of 0.75".

So, before installing the pipe with these dimensions, it is necessary to do a check for chocking.

$$\text{Chocking pressure } P^* = 2.3 \cdot \frac{d^2 * P_0^2}{l}$$

$$P^* = 2.3 \cdot \frac{0.74^2 * 2^2}{120} \approx 42 \text{ mtorr}$$

Since P^* is still lesser than 100 mtorr (assumed pressure downstream), chocking will not occur.

Now, let's check the type of flow that would occur in the system.

Knudsen number is given as

$$K_n = \frac{l'}{d}$$

l' = mean free path of the gas

d = pipe diameter

$$K_n = \frac{l_p'}{d \cdot p} \quad \text{Where } l_p' = \text{variation of } l' \text{ with respect to pressure expressed in cm.mbar}$$

For air at T=293 K, $l_p' = 6.5 \times 10^{-3}$ cm-mbar

Hence,

$$Kn = 1.3 \times 10^{-3} < 0.01$$

So, the flow comes under viscous continuum.

Calculation for Reynold's number to determine if the flow is turbulent or laminar.

$$R_e = \frac{4 \cdot q_{pv} \cdot M}{\pi \cdot d \cdot \eta \cdot R \cdot T}$$

$$R_e = \frac{4 \cdot 0.0133 \cdot 29}{\pi \cdot 1.8796 \cdot 10^{-2} \cdot 1.82 \cdot 10^{-5} \cdot 8314 \cdot 293}$$

$$R_e = 1158.35 < 2300$$

Thus, the flow is laminar.

Appendix C

Vacuum Chamber

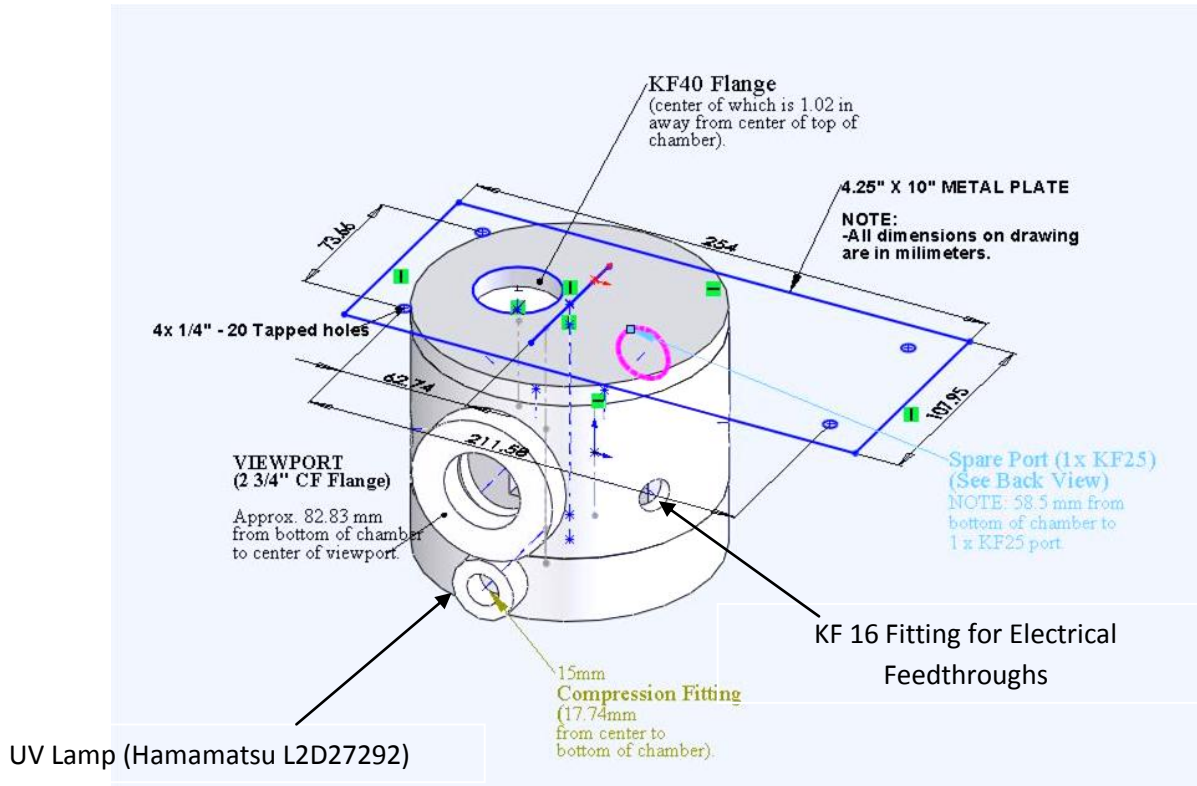


Figure C1: - Plasma Chamber

Figure C1 represents the schematic drawing of the chamber that is used to generate plasma. It is provided with 2 KF16 Fittings for inserting electrical feed-throughs, for doing four wire resistance measurements. UV lamp can be directly fit from the front of the chamber by making the use of 15mm compression fitting. KF 25 port is provided for attaching a pressure gauge while KF40 flange helps in attaching the plasma source generator to the chamber.

Appendix D

Lifting Structure

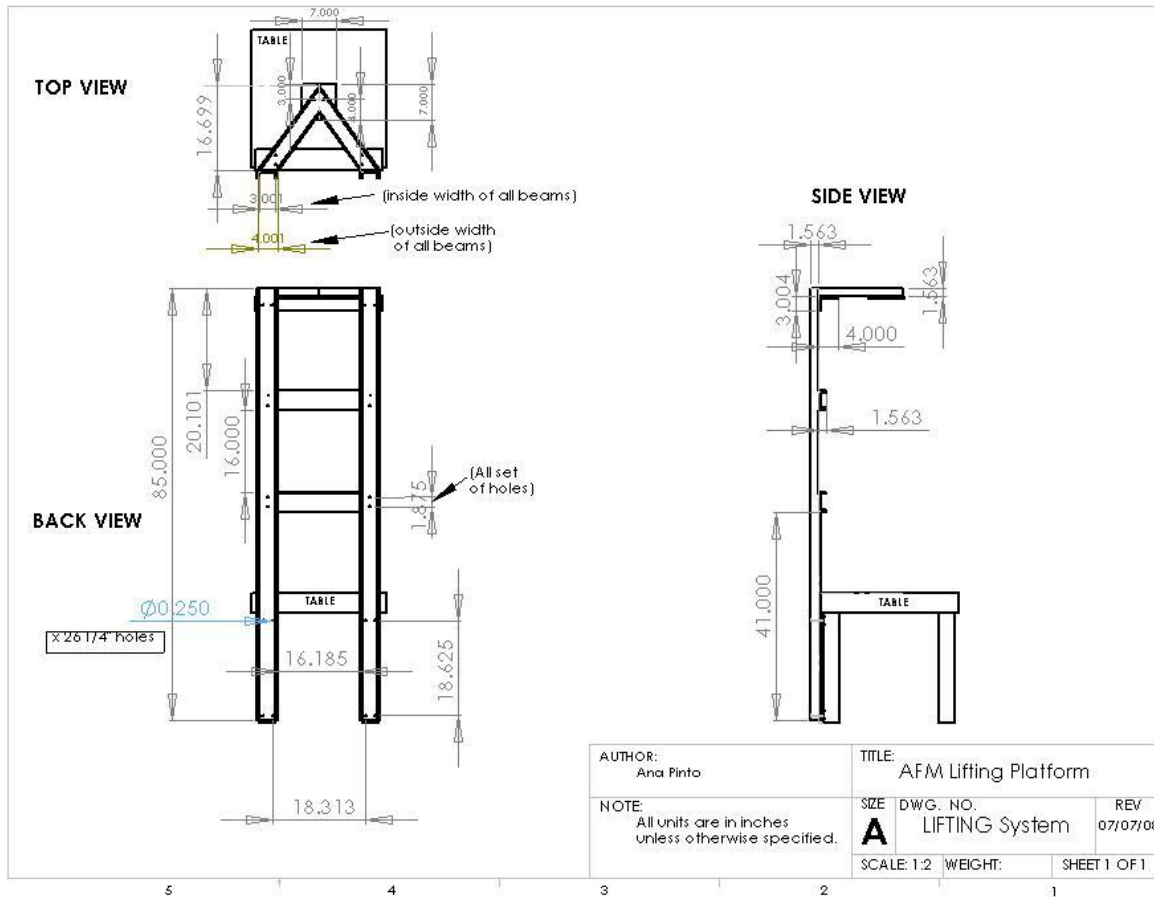


Figure D1 Lifting Structure

Figure D1 shows the drawing of the lifting structure that is connected at the back of JEOL SPM.

Three horizontal bars provided on the structure support pulleys that guide a metallic rope from winch to the plasma source generator.

Appendix E

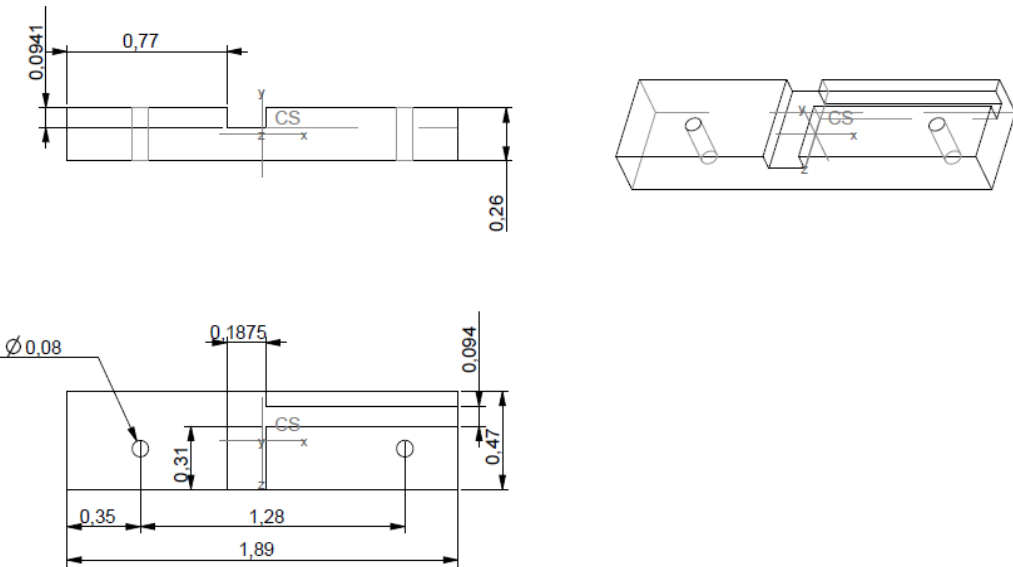


Figure E1: - Drawing of the Clamp Fixed Inside AFM for Holding N_2 Tube Near Contact

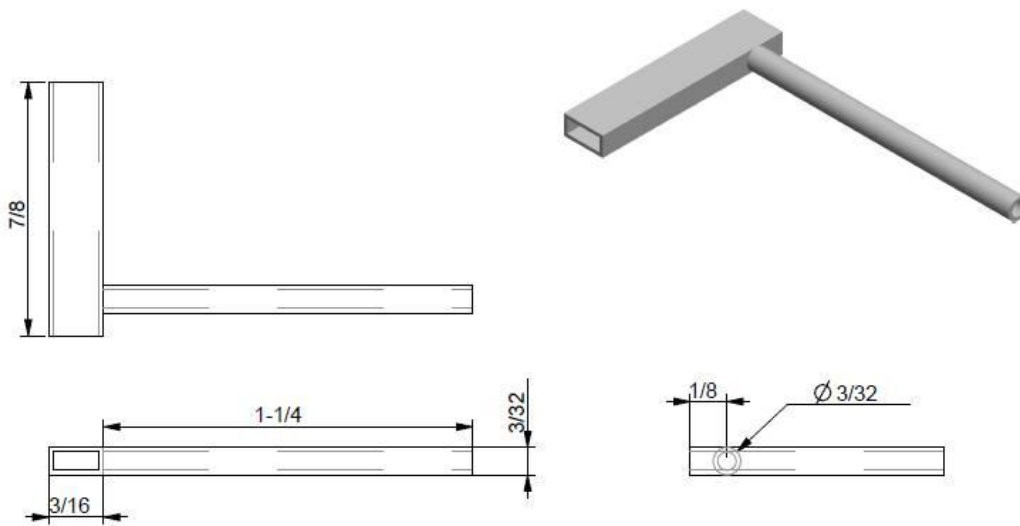


Figure E2: - Drawing of Tube Carrying N_2 Near Contact

Bibliography

1. Rebeiz, Gabriel , "*RF MEMS THEORY, DESIGN, AND TECHNOLOGY* ".
2. Milosavljevic, Zlatoljub D. , "*RF MEMS Switches : Microwave Review*" , June 2004.
3. Elliott R. Brown, "*RF-MEMS Switches for Reconfigurable Integrated Circuits*". IEEE TRANSACTIONS ON MICROWAVE THEORY AND TECHNIQUES, Novenmber 1998, Vol. 46.
4. Varadan, Vijay K.j. Vinoy K. A. Jose, "*RF MEMS AND THEIR APPLICATIONS*"
5. Chen, Dr. Lei, "Contact Evolution in Micromechanical Switches: an experimental investigation using a contact test station", Northesirtheastern University,PhD thesis ,Aug 2007.
6. Sumit Majumder, N.E. McGruer, Geroge G Adams, P.M. Zavrasky, Richard Morrison, Jacqueline Krim, "*Study of contact in an electrostatically actuated microswitch*" A 93 (19-26), s.l. : ELSEVIER, 2001, Vol. Sensors and Actuators .
7. Chow, Linda L. W., "*Lifetime Extension of RF MEMS Direct Contact Switches in Hot Switching Operations by Ball Grid Array Dimple Design*" s.l. : IEEE ELECTRON DEVICE LETTERS, June 2007, Vol. 28.
8. Qing Ma, Quan Tran, Tsung-Kuan A. Chou, John Heck, Hanan Bar, Rishi Kant and Valluri Rao, "*Metal contact reliability of RF MEMS Switches*" s.l. Intel Corporation, Santa Clara, CA 95054.

9. Feixiang Ke, Jianmin Miao, and Joachim Oberhammer, "A Ruthenium-Based Multimetal-Contact RF MEMS Switch With a Corrugated Diaphragm" s.l. : JOURNAL OF MICROELECTROMECHANICAL SYSTEMS,, Dec 2008, Vol. 17.
10. Kim, Yong Shi and Sang-Gook, "A Lateral, Self-cleaning, Direct Contact MEMS Switch" s.l. : IEEE MEMS, 2005.
11. Hyouk KWON, Jae-Hyoung PARK3, Hee-Chul LEE4, Dong-Jun CHOI, "Investigation of Similar and Dissimilar Metal Contacts for Reliable Radio Frequency Micromechanical Switches" 2008, s.l. : Japanese Journal of Applied Physics, 2008, Vols. 47, No. 8, pp. 6558–6562.
12. T. Umemoto, T. Takeuchi, and R. Tanaka, "The behavior of surface oxide film on ruthenium and rhodium plated contacts" s.l. : IEEE Trans.Compon., Hybrids, Manuf. Technol, Mar. 1978., Vols. vol. CHMT-1, no. 1,pp. 103–107.,
13. S. Umemura, K. Yasuda, and T. Aoki, "Contact resistance characteristics of noble metal alloys for connector contacts" , s.l. : IEEE Trans.Compon., Hybrids, Manuf. Technol, March 1992, Vol. vol. 14 pp. 181–186.
14. Z Yang, D Lichtenwalner, A Morris, S Menzel, "A new test facility for efficient evaluation", s.l. : JOURNAL OF MICROMECHANICS AND MICROENGINEERING 2007, Vols. 17 (1788–1795).
15. Kevin W. Gilbert¹, Shankar Mall¹, Kevin D. Leedy², Bryan Crawford, "A Nanoindenter Based Method for Studying MEMS Contact Switch Microcontacts" s.l. : Holms Conference, 2008.

16. . Esa M. Yunus, John W. McBride, and Simon M. Spearing, "*The Relationship Between Contact Resistance and Contact Force on Au-Coated Carbon Nanotube Surfaces Under Low Force Condition*", No.3 s.l. : IEEE TRANSACTIONS ON COMPONENTS AND PACKAGING TECHNOLOGIES, SEPTEMBER 2009, VOL. 32.
17. Daniel J. Dickrell, III and Michael T. Dugger, "*Electrical Contact Resistance Degradation of a Hot-Switched Simulated Metal MEMS Contact*", NO. 1, s.l. : IEEE TRANSACTIONS ON COMPONENTS AND PACKAGING TECHNOLOGIES,, MARCH 2007, Vol. VOL. 30.
18. A. Belkind, S. Gershman, "*Plasma Cleaning of Surfaces*. s.l. : Vacuum technology and coating", 2008.
19. T. García, E. Nascimento, E. Bittencourt, "*Plasma Processes as a CleanerAlternative for Cleaning, Corrosion Resistance, and Functionalization of Metallic Surfaces*", s.l. : International Workshop in Cleaner Production, Vol. 2.
20. *Remote RF Oxygen Plasma Cleaning of the Photoresist Residue and RIE-Related Fluorocarbon Films*. 2, s.l. : Journal of the Korean Physical Society,, Aug 2002, Vol. 11.
21. Manual *Plasma Cleaning of electronic materials*. s.l. : AST Products Inc.
22. VIG, JOHN R., "*UV/ Ozone Cleaning of Surfaces*", s.l. : IEEE TRANSACTIONS ON PARTS, HYBRIDS, AND PACKAGING, VOL, DECEMBER 1976, Vols. VOL. PHP-12, NO. 4.
23. Suzanne Conroy, Ron Nickerson, Min-Shyan Sheu, "*Plasma Cleaning of Medical Devices*", June 2000.

24. Soo Young Kim, 1 Kihyon Hong,1 Kisoo Kim,1 Hak Ki Yu,1 Woong-Kwon Kim,1 and Jong-Lam Lee1, "Effect of N₂, Ar, and O₂ plasma treatments on surface properties of metals" s.l. : JOURNAL OF APPLIED PHYSICS, 2008, Vols. 103, 076101.
25. [www.allaboutcircuits.com](http://www.allaboutcircuits.com/vol_1/chpt_8/9.html). [Online] http://www.allaboutcircuits.com/vol_1/chpt_8/9.html.
26. Slade, Paul G. "Electrical Contacts Principles and Applications", s.l. : Marcel Dekker, Inc.
27. H. Eid, L. Chen, N. Joshi, N. E. McGruer, G. G. Adams, "Contact And Adhesion of Elastic-plastic Layered Microsphere", San Francisco, California, USA : Proceedings of the STLE/ASME 2010 International Joint Tribology Conference, October 17-20, 2010,.
28. Lloyd, David H. [hypertextbook.com](http://hypertextbook.com/facts/2004/JennelleBaptiste.shtml). [Online]
<http://hypertextbook.com/facts/2004/JennelleBaptiste.shtml>.
29. Manual, Ansys 11.0 Reference.
30. *The interrelation between adhesion, contact creep, and roughness on the life of gold contacts in radio-frequency microswitches*. s.l. : JOURNAL OF APPLIED PHYSICS, 2006.
31. Kevin W. Gilbert1, Shankar Mall1, Kevin D. Leedy2, Bryan Crawford, "A Nanoindenter Based Method for Studying MEMS Contact Switch Microcontact", s.l. : Holms Conference, 2008.
32. Tomomi Sakata, Yuichi Okabe, Kei Kuwabara, Norio Sato, Kazuyoshi Ono, "Surface Cleaning of Gold Structure by Annealing during Fabrication of Microelectromechanical System Devices", s.l. : Japanese Journal of Applied Physics, 2009, Vol. 48 (2009) 026501.
33. www-bsac.EECS.Berkeley.EDU.

<http://www-bsac.EECS.Berkeley.EDU/~pister/245/>.

34. Ming-Tzer Lin a, Richard R. Chromik b, Nicholas Barbosa III b, Paul El-Deiry b, Seungmin Hyun b, "The influence of vanadium alloying on the elevated-temperature mechanical properties of thin gold film", 515 (2007) 7919–7925, s.l. : Science Direct, 2007.
35. Morris, D. J. Hucknall A. "Vaccum Technology calculations in chemistry". s.l. : RS.C.
36. Riviere, A. H. Rurnbull R. S. Barton J.C. "AN INTRODUCTION TO VACUUM TECHNIQUE". s.l. : Wiley.
37. Manual, DI SPM. s.l. : Veeco Metrology group.
38. [www.astricon.net](http://www.astricon.net/topics/broadband-mobile/articles/12581-rf-mems-switches-deliver-early-promise.htm). [Online] <http://www.astricon.net/topics/broadband-mobile/articles/12581-rf-mems-switches-deliver-early-promise.htm>.
39. Mr. Vince Sieracki- Naval Air Systems, "Advances in MEMs for RF Technology", s.l. : 2000 AOC Radar and EW Conference Session 2:Technology Developments & Impact on Radar/ESM, Oct 2000.
40. L. Chen, Z.J. Guo, N. Joshi, H. Eid, G.G. Adams and N.E. McGruer, "An SPM-Based Contact Tester For Study Of Microcontacts", South Carolina USA : Hilton Head, June 2010.
41. L. Chen, H. Lee, Z. Guo, N.E.McGruer, K.W. Gilbert, S. Mall, L.D. Leedy, G.G. Adams, "Contact Resistance Study of Noble Metals and Alloy Films Using a Scanning Probe Microscope Test Station," Journal of Applied Physics, Vol. 102, 2007 074910, pp. 1-7.
42. Nawaf H. Saed, "Effect of Oscillating Jet Velocity on the Jet Impingement Cooling of an isothermal surface" Scientific Research, Engineering, Nov 2009, 1, 133-139

43. <http://www.lmnoeng.com/fluids.htm>

44. <http://www.i-micronews.com/interview.asp?id=25>